https://doi.org/10.5194/egusphere-2026-541
Preprint. Discussion started: 13 February 2026
© Author(s) 2026. CC BY 4.0 License.

Nonlinear resonance in the wave–shoreline system: mechanisms and global expression

Marius Aparicio*[1], Julien Boucharel[2], Laurent Lacaze[1], and Rafael Almar[2]
[1]Univ Toulouse, Toulouse INP, CNRS, IMFT, Toulouse, France
[2]LEGOS (CNRS-IRD-CNES-University of Toulouse), Toulouse, France

Abstract. Shoreline variability is commonly interpreted through linear links with external forcings, yet many coastal systems display oscillatory modes whose origin cannot be traced to any single forcing frequency. Here, we show that a robust and regionally recurrent quasi-biennial (20–30 month) mode of shoreline variability emerges from a nonlinear triadic resonance between the semi-annual (≈6 month) components of wave energy and the corresponding delayed shoreline response. Using satellite-derived shoreline time series (1993–2019), a set of known environmental drivers, and an iterative cross-EOF method to remove all linear forcing contributions, we identify a persistent residual peak centered at 24–26 months that is absent from the forcing spectra themselves. This peak arises from resonance between two near semi-annual frequencies, specifically through excitation of the shoreline by semi-annual wave forcing that produces a phase-shifted (lagged) near semi-annual shoreline response. The semi-annual wave forcing originates from two mechanisms: (1) phase opposition between local wind-sea and remote swell along eastern boundary systems, and (2) asymmetric annual wind forcing in monsoonal regions and semi-enclosed basins. A global triadic phase-coupling analysis confirms that these near semi-annual components interact nonlinearly to inject energy at the difference frequency, producing the emergent ≈24-month mode, which represents, on average, 15% of the total dataset's shoreline variance in resonance-prone regions. These results establish nonlinear resonance as a fundamental and previously overlooked mechanism shaping shoreline variability at regional scales, with implications for understanding and predicting coastal response to changes in storm seasonality and wave-climate asymmetry.

1 Introduction

In the mid-eighteenth century, the composer Giuseppe Tartini reported a notable acoustic phenomenon: when two notes of different frequencies are played simultaneously on a violin, listeners perceive a third tone whose frequency corresponds to the interaction between the two (Tartini, 1754). This combination tone, generated by the nonlinear response of the human auditory system (Barral and Martin, 2012), is one of the earliest documented examples of nonlinear resonance. The underlying principle has found echoes far beyond acoustics, as nonlinear phase coupling plays a key role in the emergence of complex dynamics from interacting oscillatory components (Amman et al., 1941; Brown, 2011; Nayfeh and Mook, 2024).

In geosciences, the idea that environmental signals can interact to produce emergent frequencies is equally relevant. Many natural systems are driven by multiple oscillating forcings acting on different timescales, and their resulting dynamics often

---

*Corresponding author: marius.aparicio@imft.fr display nonlinear characteristics (e.g. threshold responses, alternative stable states, or road to chaos). Such behavior has been documented in coastal shallow systems (McGlathery et al., 2013), in interactions between climate modes and the annual cycle (Jin et al., 1994; Stuecker et al., 2013; Boucharel and Jin, 2020; Jiang et al., 2023), and in ecosystem responses to climatic variability (Burkett et al., 2005; Linscheid et al., 2020).

Yet, in coastal geomorphology, where sandy beaches continuously adjust to waves, tides, river discharges, and climate oscillations, this nonlinear perspective has received comparatively little attention. Most previous studies have adopted a linear cause–effect framework, correlating shoreline change directly with individual drivers such as wave energy, sea-level anomalies, or climate indices (Almar et al., 2023; Warrick et al., 2025; Graffin et al., 2025a). While these approaches have substantially advanced our understanding of coastal dynamics, they implicitly assume that shoreline variability can be decomposed into independent responses to distinct forcings.

However, beaches respond to environmental forcing with delays and memory effects (Davidson et al., 2013; Turki et al., 2012), raising the possibility that the shoreline does not merely track external variability, but may interact nonlinearly with the forcing itself. In such a framework, emergent modes of variability could arise that cannot be attributed to any single frequency of the driver. This idea is supported by recent work highlighting combination tones arising from the synchronization between the El Niño–Southern Oscillation and the seasonal cycle, which imprint on wave forcing (Almar et al., 2023; Boucharel et al., 2021), suggesting that nonlinear interactions between climate modes can propagate into coastal systems.

Independent evidence that coastal morphodynamic systems may exhibit intrinsic temporal scales beyond direct forcing has also been reported. In particular, intersite analyses of nearshore sandbar dynamics have revealed a wide range of characteristic interannual timescales that vary substantially between sites and cannot be conclusively related to differences in external forcing conditions (Ruessink et al., 2003). These findings support the interpretation of nearshore morphology as a forced, nonlinear dissipative system, in which internal dynamics can generate site-specific temporal behavior rather than a unique, forcing-controlled response. If such intrinsic timescales exist in nearshore morphology, it is reasonable to hypothesize that similar behavior may also affect shoreline position.

Consistent with this hypothesis, observations of shoreline and nearshore bathymetric variability have occasionally revealed interannual oscillations whose origin remains unresolved. Using singular spectrum analysis of long-term observations at Duck, North Carolina, Magar et al. (2012) identified recurrent oscillatory components with periods of approximately 2 years. These signals were not spatially coherent across the nearshore zone and could not be robustly attributed to wave climate, sea-level variability, or large-scale climate indices. The existence of such unexplained near-biennial variability highlights an unresolved gap in our understanding of shoreline dynamics and motivates the exploration of nonlinear and internal mechanisms.

Progress on this question has long been limited by observational constraints, as traditional coastal monitoring relies on site-specific surveys with restricted spatial coverage and limited temporal continuity (Smith and Benson, 2001; Turner et al., 2016; Ludka et al., 2019; Banno et al., 2020), making it difficult to detect nonlinear frequency couplings that require long, continuous, and spatially consistent datasets.

The recent development of satellite-derived shoreline (SDS) datasets (Vos et al., 2020, 2023b; Almar et al., 2023; Graffin et al., 2025a, b; Luijendijk et al., 2018; Castelle et al., 2023; Konstantinou et al., 2023; Turner et al., 2021) now offers a

https://doi.org/10.5194/egusphere-2026-541
Preprint. Discussion started: 13 February 2026
© Author(s) 2026. CC BY 4.0 License.

unique opportunity to revisit this problem. Multi-decadal, globally consistent observations of shoreline position enable the investigation of nonlinear interactions between coastal morphology and environmental forcings at regional scales, moving beyond site-specific correlations to assess whether shorelines exhibit resonance-like behavior driven by interacting forcings and lagged responses.

In this study, we identify a nonlinear triadic phase coupling between the semi-annual frequency of wave energy ($f_1 \approx [0.14 - 0.2]\ \mathrm{month}^{-1}$; periods of $\approx$ 5-7 months) and a lagged shoreline response of similar frequency interval ($f_2 \approx [0.14 - 0.2]\ \mathrm{month}^{-1}$). This interaction generates an emergent frequency $f_3 = |f_1 - f_2| \approx [0.031 - 0.048]\ \mathrm{month}^{-1}$, corresponding to periods of approximately 21-32 months, detectable at regional scales.

We further show that the semi-annual shoreline response arises from two distinct mechanisms: (1) a semi-annual phase shift between swell and wind-wave forcing impacting the coast, and (2) asymmetries in the annual cycle associated with anticipated or delayed storm seasons, particularly in tropical cyclone–affected basins and semi-enclosed seas. Overall, our results indicate that approximately 15% of the dataset's regional shoreline variability can be attributed to this nonlinear combination tone, underscoring the importance of nonlinear phase coupling in coastal morphodynamics.

The remainder of the paper is structured as follows. Section 2 describes the datasets and the methodology used to detect significant resonance. Section 3 presents the main global-scale results, including *in situ* comparisons and an analysis of the physical mechanisms driving resonance excitation frequencies. Section 4 summarizes the main implications of this work and outlines future research perspectives. Section 5 acknowledges the limitation of the present work. Section 6 concludes the paper.

2 Methods

2.1 Dataset and signal processing

2.1.1 Shoreline dataset

The shoreline dataset, S [m], analyzed here extends over roughly $\sim 1.5 \times 10^6$ km of global coastline, aggregated both regionally and seasonally (covering 3-month intervals and 3° alongshore) with an average alongshore sampling resolution of 0.27°. Each transect reflects the mean of waterlines detected within a 500-meter buffer, derived from 30-meter imagery. By increasing the number of aggregated observations, the detection threshold is lowered, and uncertainty is reduced. While the individual sampling Root Mean Square Error (RMSE) is typically around 10–15 meters (Vitousek et al., 2023), this approach achieves a minimum detectable shoreline change of $\Delta X_{95\%} \simeq$ 0.5–1 meter. Following Almar et al. (2023), monthly shoreline positions were extracted for 1993–2019 using the SDS framework. This method applies the Normalized Difference Water Index (NDWI) to Landsat 5, 7, and 8 imagery processed on the Google Earth Engine. The detected waterline, defined as the instantaneous land–sea interface, is used as a proxy for shoreline position. Recent multi-scale validation along the U.S. west coast (Almar et al., in review) confirmed the reliability of SDS time series across scales, from high-resolution (200 m) to coarser products ($\sim$25 km). The validation was performed against a tide-corrected high-spatial resolution dataset itself benchmarked against sparse *in situ* sites (Graffin et al., 2025a). This assessment demonstrated that even coarse-resolution SDS captures seasonal to interannual shoreline variability over regional scales ($\sim$600 km).

One limitation of SDS is the absence of tidal correction, as well as issues of SDS methods with large tidal range sites (Graffin et al., 2025b), which can add positional uncertainty in meso- to macrotidal settings (Warrick et al., 2024; Konstantinou et al., 2023). To minimize this effect, we restricted the analysis to microtidal coasts (tidal range < 2 m), where positional uncertainties typically remain within 5–10 m (Sánchez-García et al., 2020; Vos et al., 2023b; Bergsma et al., 2024). This filtering ensures that shoreline changes mainly reflect morphodynamic responses rather than tidal artifacts.

To further refine the dataset toward dynamic sandy coasts, a multi-step spatial filter was applied.

To increase the significance of our analysis, an additional multi-step spatial filter was applied to isolate open, sandy coasts. Estuaries and sheltered, low-energy environments were removed using a spatial density mask, while muddy shorelines (about 15% of the global coast) were excluded following the classification of Hulskamp et al. (2023). The resulting dataset spans $\sim 7.4 \times 10^4$ km of sandy shoreline, providing a robust basis for regional to global analyses of SDS variability.

2.2 External forcings dataset

Offshore wave conditions were obtained from the extensively validated ERA5 reanalysis (Hersbach, 2018; Dee et al., 2011; Sterl and Caires, 2005), which provides a globally consistent dataset at hourly resolution. Significant wave heights (H_s) for 1948–2018 were extracted twice a day (at 00:00 and 12:00 UTC), interpolated onto the grid of the SDS dataset, and used to compute monthly mean wave energy (E_w [J·m^{-2}]) as:

$$E_w = \frac{1}{16}\rho g H_s^2, \tag{1}$$

where ρ is the seawater density and g the gravitational acceleration.

Sea level anomalies (SLA [m]), defined as departures from long-term regional mean sea level estimated with a 5-month running average, were derived from the multi-mission satellite altimetry product SSALTO/DUACS (Pujol et al., 2016) further completed with modeled atmospheric effects (Carrere et al., 2022) also known as "storm surge". This aggregated SLA captures variability arising from diverse processes, including barotropic responses to winds and pressure, coastal upwelling, tidal residuals, and large-scale geostrophic circulation. For consistency with shoreline observations, SLA time series were interpolated onto the SDS transect locations.

Continental freshwater fluxes ([m^3.s^{-1}]) were extracted from the ISBA–CTRIP land surface–hydrology model (Decharme et al., 2019). This coupled system, validated using multiple databases of in-situ daily measurements collected from large rivers in diverse environments, resolves surface water and energy budgets (ISBA) and routes total runoff through river networks to the ocean (CTRIP), yielding daily discharge fields at 0.5° resolution since 1979. To match the shoreline record, monthly resolved discharges were interpolated onto the SDS transects for 1993–2019. Co-locating river discharge and shoreline data enables direct assessment of fluvial influence on coastal dynamics, both through sediment supply to the littoral system and through buoyancy-driven modifications of local sea level near river mouths.

https://doi.org/10.5194/egusphere-2026-541
Preprint. Discussion started: 13 February 2026
© Author(s) 2026. CC BY 4.0 License.

Finally, to account for the influence of large-scale climate variability on shoreline dynamics (Almar et al., 2023; Vos et al., 2023a; Graffin et al., 2025a), we considered several climate indices: the North Atlantic Oscillation (NAO), the Southern Annular Mode (SAM), and the El Niño–Southern Oscillation (ENSO) (Wolter and Timlin, 1998; Hurrell, 1995; Marshall, 2003). Moreover, ENSO variability was represented by the Niño3.4 index, together with its two leading spatial expressions, the Eastern Pacific (E) and Central Pacific (C) modes, derived from the first two rotated principal components of the EOF analysis of interannual SST anomalies (Takahashi et al., 2011). Finally, to investigate possible resonant or compound effects due to the ENSO C-mode variability (Stuecker et al 2013), we further defined the following seasonally modulated indices:

$$E_{\text{comb}}(t) = E(t)\cos\left(\frac{2\pi(t-T_0)}{T_{\text{year}}}\right), \qquad C_{\text{comb}}(t) = C(t)\cos\left(\frac{2\pi(t-T_0)}{T_{\text{year}}}\right), \tag{2}$$

where T_0 is a reference phase (fixed at November as ENSO peaks in boreal winter) and $T_{\text{year}} = 12$ months. These combined indices capture the interaction between interannual ENSO variability and the seasonal cycle (Boucharel and Jin, 2020).

2.2.1 Extraction of a deseasonalized residual shoreline signal

The objective of this signal processing step is to isolate shoreline variability that is not directly attributable to known external forcings, in order to investigate whether an emergent frequency f_3 arises from internal or nonlinear interactions rather than from any individual hydro/morphodynamic or climate driver. To this end, the shoreline signal must be decomposed so that residual variability reflects departures from linear, seasonally forced behavior.

The detrended satellite-derived shoreline position (SDS), denoted $S(t)$, and the forcing time series (hereafter referred to as $X_i(t)$, where the index i denotes the different environmental drivers considered in the study and described in the previous section) were first smoothed using a 3-month running average. This operation reduces high-frequency variability associated with short-lived events and measurement noise, while preserving intra-seasonal to interannual variability relevant to the targeted frequency range.

All time series were then interpolated onto a common monthly time axis to ensure temporal consistency across datasets. Prior to further analysis, each signal was normalized by its standard deviation. This normalization prevents differences in variance across forcings from biasing subsequent analyses and ensures that the extraction of residual variability is driven by dynamical relationships rather than by amplitude differences between signals.

SDS time series were deseasonalized using a monthly mean climatology estimated within a $(2K+1)$-year sliding window, with K an integer, to account for the seasonal cycle inter-annual modulation (e.g., Boucharel et al. (2013)). For each monthly-based time step t, a mean seasonal signal $\langle S\rangle_{\text{clim}}(t)$ was thus computed as:

$$\langle S\rangle_{\text{clim}}(t) = \frac{1}{2K+1}\sum_{j=-K}^{K} S(t + j \times 12\text{-month}) \tag{3}$$

Here $K = 1$ was chosen, i.e. a ±12-month sliding windows (Fig. 1). Various sliding window ranges were tested (3- to 7-years) without showing significant differences. The one retained here was chosen for its compromise between sufficient temporal extension to capture seasonal cycle variability and shortness to avoid losing signal amplitude within each seasonal oscillation.

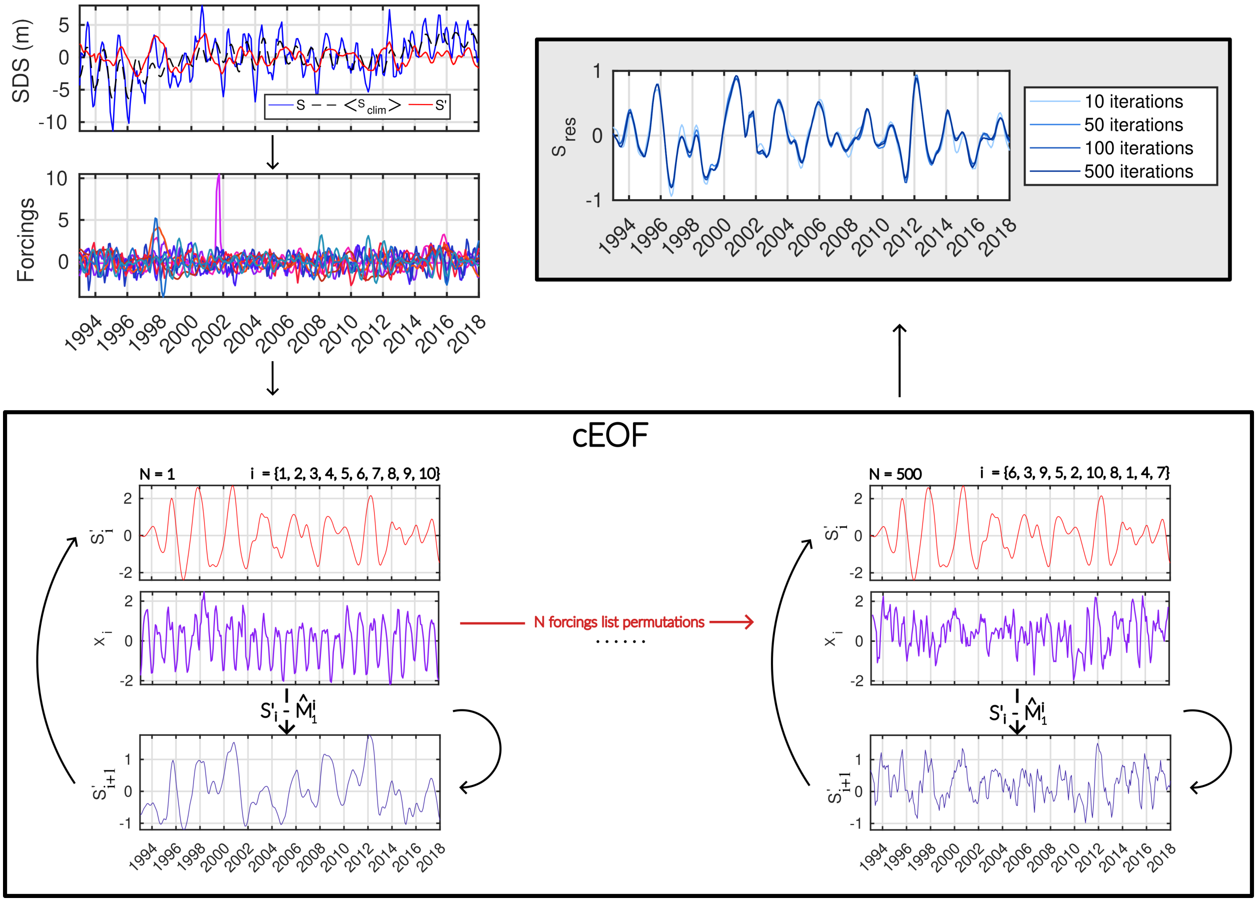

Figure 1. Illustration of the signal processing method used to remove the linear influence of all forcings from SDS signals. First, the seasonal climatology ($\langle S\rangle_{clim}(t)$), dynamically computed over a 2-year window, is removed from the original SDS signal ($S(t)$) to obtain $S'(t)$. Then, the forcing list $X_i(t)$ is used iteratively: the first EOF mode of forcing X_i is computed with $S'_i(t)$ and removed from it, producing the signal $S'_{i+1}(t)$. This signal is then used with the next forcing in the list, and so on. To avoid the influence of forcing order on the final residual signal, a Monte Carlo procedure is applied by computing K random permutations of the forcing list. The K resulting iterations are then averaged to generate the final residual signal S_{res}. Tests showed that convergence is reached for $K \geq 100$; here, $K = 500$ was chosen.

The deseasonalized shoreline anomaly is then:

$$S'(t) = S(t) - \langle S\rangle_{\text{clim}}(t) \qquad (4)$$

Shoreline anomalies were subsequently band-pass filtered with a 4th-order Butterworth filter (Roberts and Roberts, 1978), retaining 6–48 month periods to remove long-term interannual variability (≥ 5 years) that would be to long for the time window available. Regional aggregation, necessary to reduce spatial noise and account for coasts with similar wave orientations, was

https://doi.org/10.5194/egusphere-2026-541
Preprint. Discussion started: 13 February 2026
© Author(s) 2026. CC BY 4.0 License.

performed according to transect neighbors' bearing angles (θ). The bearing angle was averaged over a $D = 500$ km radius, and sites within $\delta\theta = \pm 15°$ were merged.

Finally, we isolated the component of shoreline variability independent of the known linear influence of external forcings using a cross-EOF (cEOF) iterative removal approach (Wilks, 2011; Hannachi, 2004). At each location, the residual shoreline signal $S'(t)$ was analyzed jointly with a set of potential climate and oceanic drivers $\{X_i(t)\}$, with $i = 1, \ldots, 10$ corresponding to NAO, SAM, Niño3.4, E_{ENSO}, C_{ENSO}, E_{comb}, C_{comb}, SLA, river discharge, and E_w.

At each iteration i, a cEOF decomposition between $S'_i(t)$, with $S'_0(t) \equiv S'(t)$ and a given forcing $X_i(t)$ allows identifying their leading mode, $\hat{M}_1^{(i)}(t)$, representing the part of shoreline variability linearly linked to that specific driver (Fig. 1). This mode was then reconstructed and subtracted from the shoreline signal as:

$$S'_{i+1}(t) = S'_i(t) - \hat{M}_1^{(i)}(t) \tag{5}$$

thereby progressively removing the variance associated with each forcing. The process was repeated across all 10-drivers until no significant linear covariance remained. The resulting residual series $S_{res}(t) = S'_{i=10}(t)$, thus represents the component of shoreline variability not explained by the direct, linear influence of the prescribed forcings (Fig. 1).

Because the order of removal can influence the resulting residual, we implemented a Monte Carlo ensemble strategy (Kroese and Rubinstein, 2012). In this approach, the forcings were presented in randomized order, i.e. specific value of i being associated with a random driver in the list of the 10-drivers, across N iterations ($N = 500$), and the resulting residuals were averaged to obtain a stable estimate. Convergence was evaluated by computing the root-mean-square error (RMSE) between ensembles means of increasing sizes (N=10:50:500), showing that stable convergence is achieved for $N \geq 100$. This procedure ensures that the final residual signal is robust with respect to the ordering of forcings.

To ensure that the cEOF methodology, does not introduce artificial frequencies, we applied the same routine to synthetic time series composed of white and colored noise (red and pink). The results shown in Fig. 2 indicate that the method does not generate spurious frequencies, even for temporally correlated noise, highlighting both its robustness and its unbiased nature.

At last, coastal sediment redistribution is ultimately driven by oceanic forcings. Hence, in their absence (i.e., no ocean), the beach profile would rapidly adjust toward a gravity-controlled equilibrium. Consequently, intrinsic dynamics in S'_{res} are expected to be limited, although potential feedbacks or unresolved processes cannot be fully ruled out. The remaining signal is therefore mainly composed of (1) measurement noise, (2) the nonlinear influence of forcings and morphological feedbacks, and (3) resonance-induced variability, suitable for spectral analysis.

https://doi.org/10.5194/egusphere-2026-541
Preprint. Discussion started: 13 February 2026
© Author(s) 2026. CC BY 4.0 License.

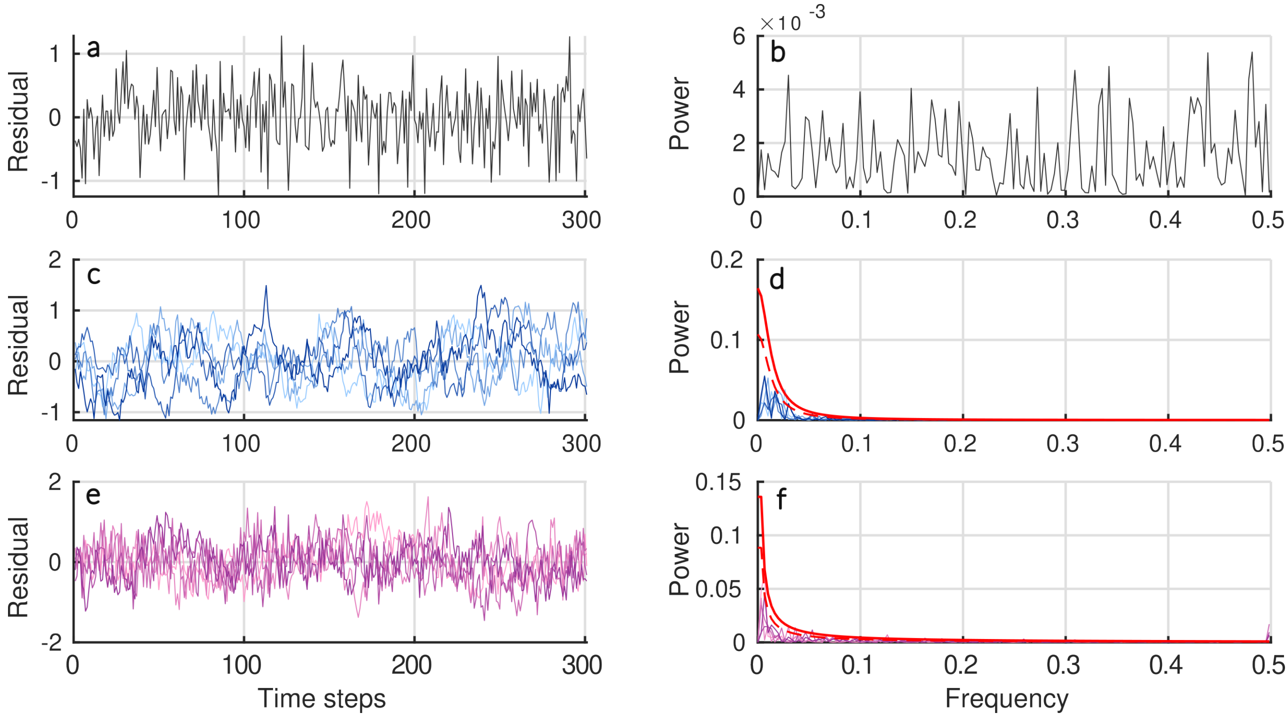

Figure 2. Averaged residuals (N = 500) and corresponding power spectra obtained after applying the cEOF methodology to synthetic noise. Left column (a, c, e): residual time series; right column (b, d, f): Fourier spectra of the residuals. (a, b) correspond to white noise, (c, d) to five realizations of red noise, and (e, f) to five realizations of pink noise. The length of the synthetic time series is comparable to the observational records (expressed in months). Red curve and dashed red curve denotes the 99 % and 95 % significance level, respectively.

2.3 Triadic phase coupling analysis

The necessary and sufficient conditions for resonance to arise are: (1) temporal phase coherence between the interacting signals, and (2) energy input at or near the system's natural frequency that is sufficient to balance dissipation (Brown, 2011). To evaluate whether shoreline variability exhibits signatures of such nonlinear resonance, we performed a triadic phase coupling analysis between three signals: (1) the high-frequency wave energy $E_w(t) \equiv x_1(t)$, (2) the high-frequency shoreline position $S(t) \equiv x_2(t)$, both filtered to retain periods $T < 7$ months to capture the semi-annual component of both signals (see Appendix A), and (3) the residual shoreline signal $S'_{res}(t) \equiv x_3(t)$, which represents variability independent of linear forcings and in which an emergent resonant frequency may be observed. In order to obtain a robust signal reconstruction suitable for triadic phase coupling analysis, it is essential to ensure that the reconstructed signals capture genuine sub-annual variability in shoreline dynamics and wave forcing, rather than artifacts arising from seasonality, noise, or methodological bias (see discussion in the previous section). To this end, a sequence of wave filtering and signal processing steps was applied to the original time series $x_i(t)$, with $i = 1, 2, 3$. These procedures were designed to isolate the frequency bands of interest while preserving the phase relationships relevant to nonlinear interaction analysis. A detailed description of the filtering strategy and associated sensitivity

https://doi.org/10.5194/egusphere-2026-541
Preprint. Discussion started: 13 February 2026
© Author(s) 2026. CC BY 4.0 License.

tests is provided in Appendix A. Finally, we note that additional coupling tests were conducted using alternative environmental drivers $X_i(t)$ $(i = 1,\ldots,9)$, distinct from the wave energy forcing E_w. No statistically significant resonances were detected in these cases. Consequently, the analysis presented hereafter focuses exclusively on the triadic coupling involving wave energy and shoreline response identified above.

The rationale underlying triadic emergence is that, if shoreline dynamics partly arise from nonlinear interactions, a frequency observed in the residual signal x_3 may result from the interaction of oscillatory components present in both x_1 and x_2. In particular, the interaction of semi-annual oscillations in these two signals can generate a combination frequency of the form: $f_3 \approx |nf_1 - mf_2|$, where n and m are integers. Such nonlinear coupling produces two complementary frequency components: a low-frequency component at $|nf_1 - mf_2|$ and a high-frequency component at $nf_1 + mf_2$. In the present case, the high-frequency component corresponds to periods approaching the Nyquist limit, defined as $P_{\text{min}} = 1/f_{\text{Nyq}} = 2$ months (Shannon, 2006), and is therefore not resolvable with the available temporal sampling. By contrast, the low-frequency component emerges clearly in the residual signal as a robust and physically interpretable mode of variability. While higher-order combinations $(n, m > 1)$ are theoretically possible in nonlinear systems, they generally correspond to weaker interactions and are rarely dominant in geophysical signals. Consequently, the analysis focuses on the lowest-order interaction $(n = m = 1)$, which is expected to capture the most energetic and physically relevant triadic phase coupling. Demonstrating this coupling requires not only the identification of spectral peaks but also confirmation of persistent phase coherence between the three signals. This is achieved by retrieving the instantaneous phase and amplitude of the signals using the Hilbert transform.

Therefore, each signal is standardized to zero mean and unit variance,

$$x'_i(t) = \frac{x_i(t) - \langle x_i \rangle}{\sigma(x_i)}, \qquad i = 1,2,3, \tag{6}$$

to enable direct comparison of their oscillatory components and to prevent differences in amplitude or physical units from biasing the subsequent analysis.

To mitigate edge effects introduced by the Hilbert transform (Pikovsky et al., 2001), n_{trim} points were removed at both ends of each time series. This trimming avoids artificial phase wrapping and spurious phase locking near the signal boundaries. In addition, a moving average of width w was applied to suppress very short-scale variability that does not contribute meaningfully to sub-annual oscillatory behavior.

The analytic representation of each normalized signal was obtained via the Hilbert transform,

$$z_i(t) = x'_i(t) + i\,\mathcal{H}[x'_i(t)] \tag{7}$$

from which the instantaneous phase and amplitude were derived as

$$\phi_i(t) = \arg(z_i(t)), \qquad a_i(t) = |z_i(t)| \tag{8}$$

Here, the phase $\phi_i(t)$ describes the timing of oscillations, while the amplitude $a_i(t)$ characterizes their instantaneous strength.

Because quasi-oscillatory signals in geophysical systems often exhibit strong temporal modulation of their amplitude, it is essential to focus the analysis on intervals during which the three signals simultaneously carry significant energy. To this end,

© Author(s) 2026. CC BY 4.0 License.

we defined a multiplicative amplitude weight,

$$A(t) = a_1(t)\,a_2(t)\,a_3(t) \tag{9}$$

Only time steps for which $A(t)$ exceeded a threshold ζ, defined as the $(1-\zeta)$ quantile of $A(t)$, were retained. This filtering step minimizes the influence of low-amplitude intervals dominated by noise and ensures that the phase coherence metrics are computed from dynamically meaningful oscillations.

For a genuine triadic interaction, the phase combination

$$\Delta\phi(t) = \phi_1(t) - \phi_2(t) - \phi_3(t) \tag{10}$$

should remain approximately constant over extended time intervals. In the absence of coupling, $\Delta\phi(t)$ behaves as a random variable uniformly distributed in $[-\pi, \pi]$, resulting in no systematic phase coherence. Conversely, nonlinear resonance manifests as a clustering of $\Delta\phi(t)$ around a preferred value, indicative of phase locking.

The degree of phase clustering was thus quantified using the amplitude-weighted coherence metric:

$$R_w = \left| \frac{\sum_t A(t)\,e^{i\Delta\phi(t)}}{\sum_t A(t)} \right| \tag{11}$$

The metric R_w approaches unity when the phase difference remains nearly constant over time, while assigning greater weight to intervals characterized by strong oscillatory energy and down-weighting noisy fluctuations.

To assess the statistical significance of the observed coherence, R_w was evaluated against a null hypothesis of no coupling. While significance levels in classical wavelet coherence studies are often derived from Monte Carlo simulations of prescribed noise processes (e.g., Gaussian white noise or AR(1) red noise; Maraun and Kurths 2004; Grinsted et al. 2004; Torrence and Webster 1999), we adopted a non-parametric permutation approach. At each iteration, the phase of $x_1(t)$ was randomly permuted while $x_2(t)$ and $x_3(t)$ were kept fixed, thereby preserving marginal distributions and amplitudes while destroying any genuine phase relationship. A surrogate coherence value $R_w^{(k)}$ was computed for each realization, and after $N_{\text{perm}} = 500$ permutations the empirical p-value was estimated as

$$p = \frac{1}{N_{\text{perm}}} \sum_{k=1}^{N_{\text{perm}}} \mathbf{1}_{\{R_w^{(k)} \geq R_w\}} \tag{12}$$

This procedure is conceptually analogous to Monte Carlo testing but has the advantage of being distribution-free, as the null distribution is constructed directly from the observed data rather than from an assumed noise model.

Because the results may depend on user-defined parameters, we systematically explored a range of values for the smoothing window w (3, 5, and 7 months), the amplitude threshold ζ (from 0.1 to 0.5), and the trimming length n_{trim} (30, 50, 70, and 90 points). For each location, all parameter combinations were tested, and the optimal configuration was selected as the one maximizing R_w among statistically significant cases ($p < 0.05$) and based on a sufficiently long record ($n_{\text{valid}} \geq 40$). The threshold on n_{valid} was determined from permutation-based null experiments, which showed that the variance of R_w stabilizes and decreases below 0.01 beyond this sample size. This ensemble strategy reduces sensitivity to arbitrary parameter choices while ensuring statistical robustness.

Finally, because the analysis relies on remotely sensed observations of real-world signals, an additional effect-size criterion was imposed by requiring $R_w > 0.5$. As emphasized by Maraun and Kurths (2004) and Grinsted et al. (2004), statistically significant coherence values can still be misleading when their magnitude is small, as they may reflect weak or intermittent interactions rather than robust coupling. Although not prescribed by existing studies, the threshold $R_w = 0.5$ represents a conservative and pragmatic choice to retain only locations exhibiting both statistical significance and physically meaningful coherence.

3 Results

3.1 Evidence of triadic frequency resonance from *in situ* dataset: Torrey Pines

The relevance of a resonant frequency ($f_3 \approx |f_1 - f_2|$) involved in shoreline evolution is first assessed using a micro-tidal *in situ* shoreline dataset from Torrey Pines (TP) Beach, California (see Fig. 3a and, e.g., Aubrey et al., 1976). The analysis covers nearly 15 years of weekly to monthly shoreline position surveys above the low-tide waterline, acquired using GPS at transect 540 (highlighted by the red solid line in Fig. 3a). The corresponding shoreline position $S_{\mathrm{TP}}(t)$, its mean seasonal cycle $\langle S\rangle_{\text{clim},\mathrm{TP}}$, the deseasonalized signal S'_{TP}, and the normalized residual signal $S'_{res,\mathrm{TP}}$ are shown in Fig. 3b. The variance of the residual signal is estimated as:

$$\mathcal{R} = \frac{\mathrm{Var}(S'_{\text{res}})}{\mathrm{Var}(S)} \times 100 \tag{13}$$

and accounts for $\mathcal{R} \approx 7\%$ of the total shoreline variance.

The wavelet power spectrum of the shoreline residual signal $S'_{\text{res},\mathrm{TP}}$ obtained after applying the cEOF methodology reveals a distinct biennial frequency peak $f^{\text{peak}}_{\mathrm{TP}}$, corresponding to a period of $T^{\text{peak}}_{\mathrm{TP}} \equiv 1/f^{\text{peak}}_{\mathrm{TP}} \approx 26$ months, which is significant above the 99% confidence level (Fig. 3c; solid red). The same peak frequency is also identified within the wavelet power spectrum of the original shoreline signal (Fig. 3c; dotted-blue), providing additional confidence that the methodology adequately removes the driver-linked shoreline frequencies without adding any spurious one. Moreover, removing the seasonal band (10–14 months) within the shoreline (Fig. 3c; solid blue) and wave energy (Fig. 3c; solid black) signals allows other frequencies to peak more distinctly, showing that both signals present a significant semi-annual peak, with the wave energy peaking at a shorter period (allowing for a slight period offset required for subtractive resonance), while also revealing that no peak is present in wave forcing around $f^{\text{peak}}_{\mathrm{TP}}$. Additionally, the associated wavelet scalogram (Fig. 3d) indicates that $f^{\text{peak}}_{\mathrm{TP}}$ corresponds to a coherent and persistent energy band over the full 15-year record, rather than to a transient or episodic fluctuation (yellow band in Fig. 3d).

Hence, to assess whether this biennial variability arises from nonlinear interactions enabled by sufficient phase coherence across time, we applied the amplitude-weighted triadic phase coherence metric R_w (Eq. (11)) to the reconstructed sub-annual components of the wave energy ($x_{1,\mathrm{TP}}(t)$) and shoreline signal ($x_{2,\mathrm{TP}}(t)$), together with the shoreline residual signal ($S'_{\text{res},\mathrm{TP}}(t) \equiv x_{3,\mathrm{TP}}(t)$). The analysis reveals a significant phase locking consistent with a triadic interaction of the form $f^{\text{peak}} \equiv f_3 \approx |f_1 - f_2|$, where f_1 corresponds to a dominant frequency in wave energy variability and f_2 to a semi-annual shore-

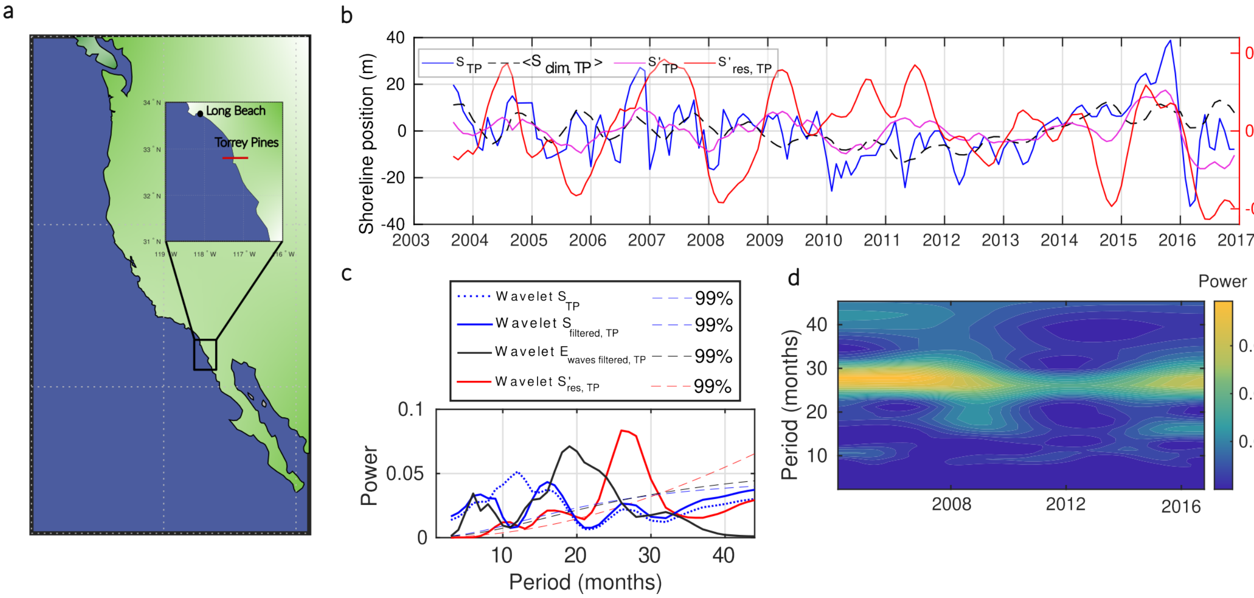

Figure 3. Residual frequency analysis at Torrey Pines after cEOF cleaning. (a) Map of the U.S. West Coast highlighting the study region in Southern California. The inset shows Long Beach and Torrey Pines, with the transect (red marker) of interest. (b) Time series of the *in situ* monitored shoreline position S_{TP} (blue), climatological seasonal cycle $S_{\mathrm{clim,TP}}$ (black dashed), deseasonalized signal S'_{TP} (pink), and normalized residual signal $S'_{res,\mathrm{TP}}$ (red), plotted on the y-axis right. (c) Spectral analysis of the Torrey Pines original signal S_{TP} (blue dotted), the original signal with the seasonal band removed ($S_{\mathrm{filtered,TP}}$; solid blue), the residual shoreline signal ($S'_{res,\mathrm{TP}}$; solid red), and the wave energy signal with the seasonal band removed ($E'_{wavesfiltered,\mathrm{TP}}$; solid black). The comparison of the global wavelet spectra reveals a distinct peak in $S'_{res,\mathrm{TP}}$ at approximately 26 months, exceeding the 95–99% confidence levels, revealing a significant quasi-biennial mode of variability that does not match any frequency peak in the wave energy signal. (d) Wavelet power spectrum of $S'_{res,\mathrm{TP}}$ as a function of time and period. The persistence of enhanced energy in the 26–28 month band across the record indicates that this oscillatory mode is temporally coherent and recurrent across the monitoring window.

line oscillation. For this site, the coherence reaches $R_w \approx 0.46$, exceeding both the statistical significance threshold ($p < 0.05$ based on permutation testing) and the minimum sample-size requirement ($n_{\mathrm{valid}} \geq 40$). This indicate that the phase difference $\Delta\phi(t)$ remains clustered around a preferred value over extended time intervals, consistent with a sustained nonlinear phase coupling.

These field observations demonstrate that the near-biennial frequency observed in the shoreline anomaly signal can arise from a nonlinear interaction between two distinct oscillatory components: a semi-annual variability in wave energy forcing and a lagged semi-annual shoreline response. Importantly, the Torrey Pines site analyzed here is later identified as a resonance-prone location in the global satellite-derived shoreline dataset (see Subsect. 3.2). This consistency between independent *in situ* observations and spaceborne measurements supports the interpretation that the resonant frequency detected at regional scales reflects a physically meaningful nonlinear process that is also observable in long-term field measurements.

3.2 Upscaling to the global scale

Building on the site-specific evidence presented above, we now assess whether the same triadic resonance mechanism can be systematically identified regionally at global scales. The objective is to determine whether the near-biennial frequency observed locally in California reflects an isolated behavior or instead emerges as a recurrent feature of shoreline dynamics across diverse coastal settings. To this end, we apply the amplitude-weighted phase coherence metric R_w to satellite-derived shoreline observations worldwide by explicitly testing for the presence of a nonlinear interaction of the form $f_3 \approx |f_1 - f_2|$ within the coupled shoreline–wave system, allowing us to evaluate the spatial prevalence, coherence, and statistical robustness of the triadic resonance identified at the field site.

Analysis of the residual shoreline signal S'_{res} indicates that a non-negligible fraction of sandy coastlines exhibits a well-defined near-biennial frequency f^{peak}, with an average period of $T^{\text{peak}} \approx 24.5$ months (Fig. 4b). This signal is predominantly observed along eastern boundary coastlines (e.g., Chile–Peru, Namibia–Angola, eastern Australia) as well as in several semi-enclosed basins, including the Caribbean Sea, the Mediterranean Sea, and the Arabian Sea (Fig. 4a). This frequency does not coincide with any dominant frequency present in the external forcing across the full extent of corresponding regions. In areas identified as resonance-prone, the variance associated with this residual signal represents on average $\mathcal{R} \approx 15\%$ of the total shoreline variance in the dataset (Fig. 4c).

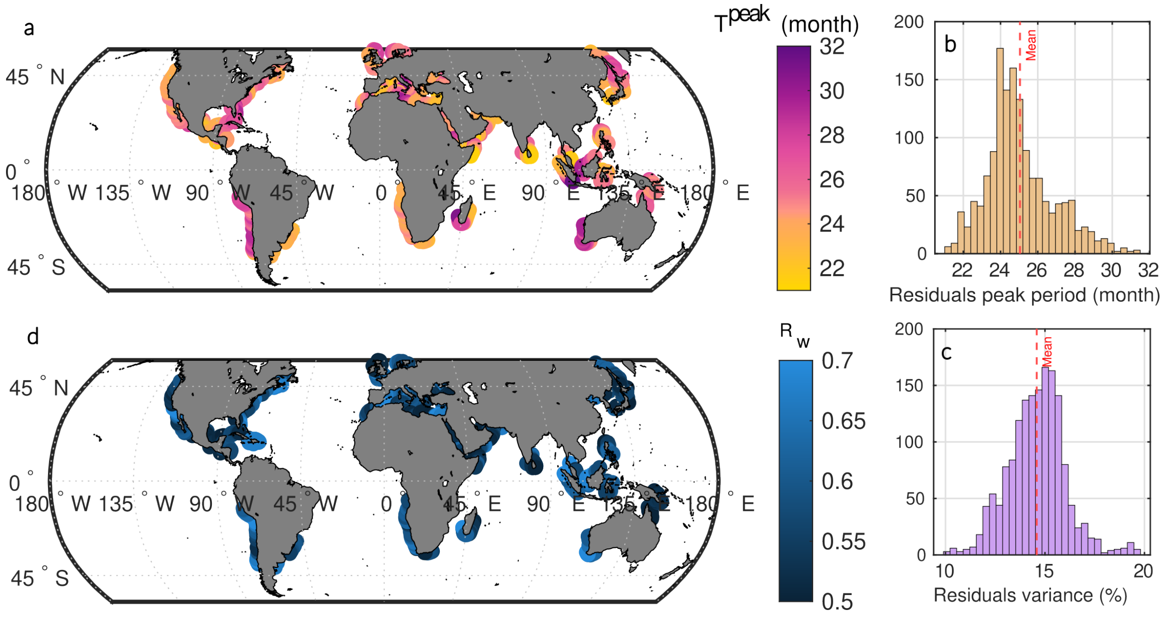

Figure 4. Global analysis of shoreline residuals S'_{res}. (a) shows the dominant spectral period (T^{peak}) of S'_{res}. (b) shows the distribution of the dominant periods T^{peak} associated with panel (a). (c) gives the distribution of the variance of S'_{res} relative to the original shoreline signal S. Red dashed lines indicating mean values. (d) presents amplitude-weighted coherence coefficient (R_w), highlighting regions of significant resonance and phase coupling between forcing and shoreline response.

The observed near-biennial frequency ($f^{\text{peak}} \equiv f_3$) is consistent with the hypothesized triadic phase interaction between a semi-annual component of the wave energy signal (f_1) and a lagged semi-annual response of the shoreline (f_2), for which the necessary conditions for nonlinear phase coupling are met. Support for this interpretation is provided by the amplitude-weighted phase coherence R_w (Fig. 4d), which reaches an average value of $R_w \approx 0.6$ across resonance-prone regions, with an interquartile range $R_w^{\text{5th–95th}} \in [0.51, 0.70]$ and statistical significance ($p < 0.05$). Such coherence values indicate a strong, phase-locked, and temporally persistent interaction between the semi-annual wave forcing and the lagged semi-annual shoreline response, consistent with the presence of a nonlinear triadic resonance mechanism.

This result does not imply that resonance is continuously active throughout the full observation period. Rather, it indicates that phase coupling occurs over a sufficiently large fraction of the record, either through extended intervals of sustained interaction or through repeated resonant episodes. The global-scale detection of this interaction further suggests that distinct regional mechanisms may give rise to similar triadic responses, all converging toward the emergence of a near-biennial shoreline variability.

3.3 Mechanisms of semi-annual oscillations in shoreline and waves

To further elucidate the physical mechanisms underlying this phase-locked semi-annual interaction, we next examine two processes through which semi-annual oscillations in wave energy and shoreline variability can be generated and combined to produce triadic resonance. These mechanisms are identified as: (1) phase shifts between distinct wave systems (wind-sea versus swell), and (2) asymmetries arising from the intrinsically non-sinusoidal nature of the local wind cycle, both of which excite the shoreline at semi-annual timescales.

3.3.1 Phase shift between local wind-sea and remote swell

Along eastern boundary coasts mostly located away from storm-track latitudes, the seasonal evolution of wave energy reflects the superposition of two distinct regimes: locally generated wind-sea and swell remotely generated within the storm-tracks. Figures 5a and 5b illustrate the global distribution of the month of maximum climatological activity for these two wave components. Along eastern boundary systems, these maps reveal a systematic seasonal offset between wind-sea and swell maxima. Specifically, during the hemispheric winter, energetic swell generated in mid- to high-latitude storm tracks propagates toward the coast, while local wind activity remains relatively weak. Conversely, during the local summer, enhanced coastal wind forcing generates energetic wind-sea events directed toward the coast, whereas swell activity decreases. As a result, the annual cycles of wind-sea and swell energy are frequently out of phase along these coastlines (Semedo, 2018; Semedo et al., 2018; García-Reyes et al., 2018).

This phase opposition is further illustrated in Fig. 5c, which shows the mean seasonal cycles of normalized wind-sea and swell energy for four representative eastern boundary regions: the North American West Coast (NAWC); the West African Coast (WAC) comprising both the Namibian, the Angolan and the Benguela coasts; the South American Coast (SAC); the Australian West Coast (AWC). In these specific regions, swell energy peaks during winter months, while wind-sea energy reaches its maximum during summer, with the two components exhibiting distinct and systematically phase-shifted annual evo-

https://doi.org/10.5194/egusphere-2026-541
Preprint. Discussion started: 13 February 2026
© Author(s) 2026. CC BY 4.0 License.

lutions. Such semi-annual modulation has been identified at the global scale in previous studies (Colosi et al., 2021; Echevarria et al., 2019). Here, we show that this modulation plays a key role in exciting a semi-annual shoreline response, which subsequently participates in the triadic resonance mechanism described above. In particular, intercomparison of Figs. 4d and 5a reveals coherent regional patterns between elevated values of the phase coherence metric R_w and regions characterized by a pronounced phase offset between wind-sea and swell. This is especially evident along eastern boundary systems such as the North American West Coast, the Namibia–Angola Coast, the Peru–Chile coast, and Western Australia.

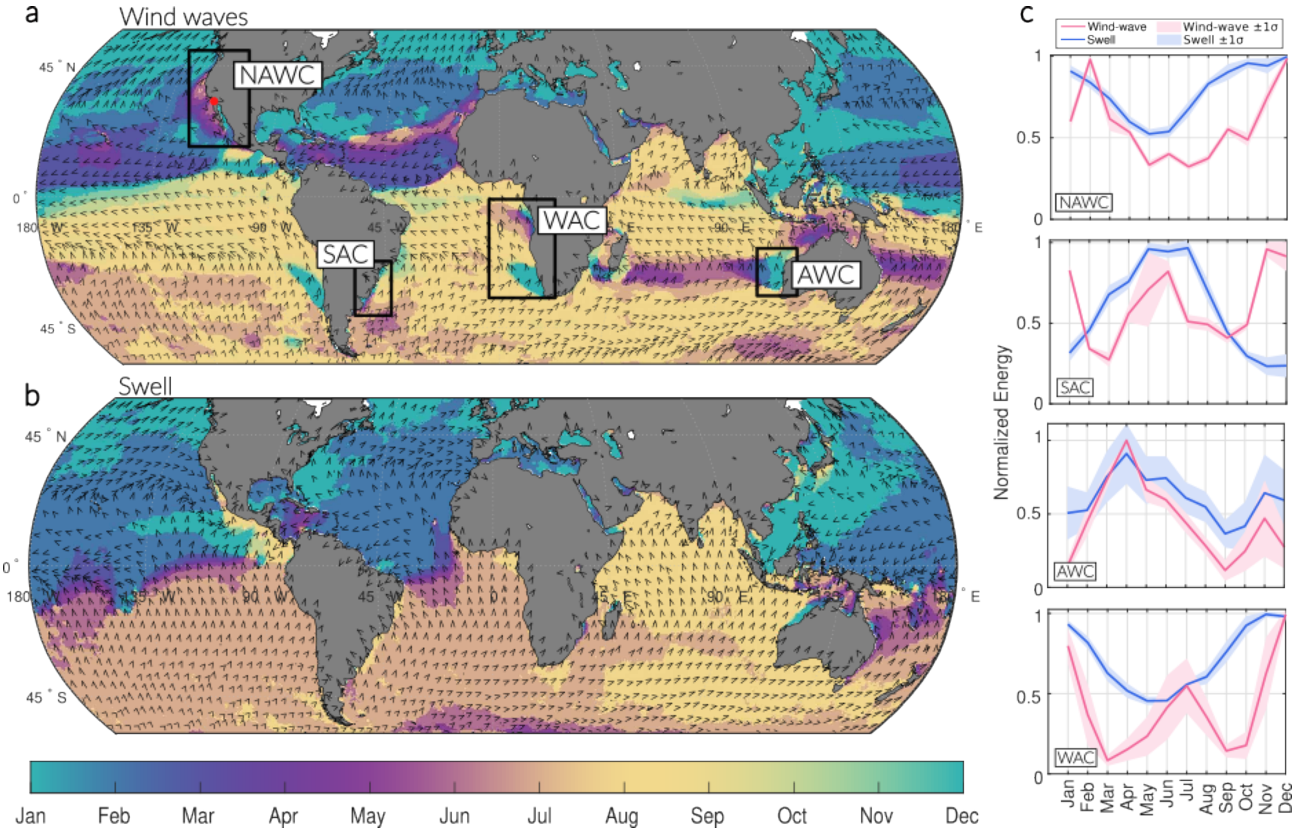

Figure 5. Monthly climatology of global wave energy regimes derived from ERA-reanalysis (1948-2018). (a) Month of maximum climatological wind-wave activity, with arrows indicating the mean wave direction at the time of the maximum. (b) Same as (a), but for swell waves. Colors represent the month of occurrence of the maximum (scale below), highlighting the seasonality of the two regimes. Black boxes delineate the North American West Coast (NAWC) and the West African Coast (WAC), which are further analyzed. The red dot highlights Torrey Pines location. These patterns emphasize the contrasting seasonal timing and directional forcing of locally generated wind waves versus remotely generated swell, underlining their distinct roles in shoreline variability and resonance. (c) Mean seasonal cycles of normalized wave energy for the 20 most swell/wind waves out of phase grid points flagged within each region (to avoid spatial oversmoothing). Shaded areas represent the signal standard deviation (± 1 σ). In all regions, wind-wave (pink) and swell (blue) regimes exhibit distinct annual peaks or, at least, two distinct peaks within a year when ERA5 reanalysis performs poorly in separating swell from wind sea.

To illustrate the implications of this semi-annual structure for shoreline dynamics, we focus in the following on four eastern boundary coastlines (NAWC, SAC, AWC, and WAC) as illustrative case studies. As previously stated, the pronounced phase offset between wind-sea and swell leads to an alternating dominance of the two components throughout the year. When both components are sufficiently energetic, their seasonal phase opposition produces a semi-annual modulation of the total coastal wave-energy spectrum, characterized by two relative maxima per year.

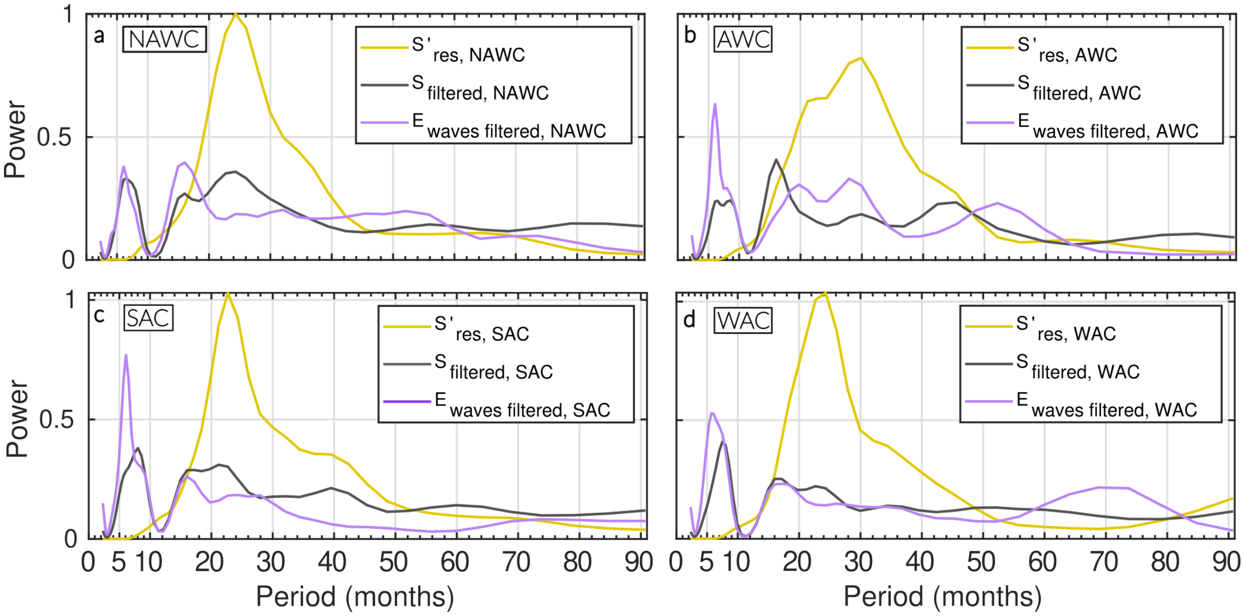

Figure 6. Regional expression of semi-annual forcing and emergent near-biennial shoreline variability along four eastern boundary systems (NAWC, SAC, AWC, WAC). For each region, the panel shows the regionally averaged power spectra of the original shoreline signal (black), the wave energy signal (pink), and the residual shoreline signal after cEOF removal (yellow). The dominant seasonal band (10–14 months) is masked to highlight secondary peaks. Across all regions, both shoreline position and wave energy exhibit a semi-annual peak, with wave energy systematically peaking at slightly shorter periods, consistent with the frequency offset required for subtractive resonance. The residual shoreline signal systematically displays a robust near-biennial peak, which is also present in the original shoreline spectrum, confirming that it represents a genuine component of shoreline variability rather than an artifact of the residual extraction. (a, c, d) For three regions (NAWC, SAC, WAC), wave energy does not exhibit a significant peak within the f^{peak} band, indicating that the emergent near-biennial shoreline variability is not directly inherited from the forcing spectrum. (d) In contrast, the AWC region shows a wave-energy peak close to, but offset from, the residual shoreline peak, suggesting a concomitant influence of band-limited wave forcing and nonlinear phase resonance.

To highlight this, we averaged the wavelet power spectrum over each region of interest for the original shoreline (black) and wave energy (pink) time series, while masking the seasonal band (10–14 months) to allow secondary peaks to emerge more distinctly in the analysis (Fig. 6). The regionally averaged wavelet spectrum of the residual shoreline signals (yellow) is also computed for comparison. The results are unambiguous: the residual peak f^{peak} is consistently present in the original shoreline

© Author(s) 2026. CC BY 4.0 License.

signal, confirming that it reflects a genuine component of shoreline variability. For all four coastal systems, both shoreline position and wave energy exhibit a semi-annual peak, with wave energy systematically associated with shorter periods, consistent with the offset required for subtractive resonance. Moreover, for three regions (NAWC, SAC, WAC), wave energy does not display any significant peak within the frequency band of f^{peak} (Fig. 6a, c-d), confirming that the main driver of shoreline variability (i.e., waves) is not responsible for the near-biennial shoreline peak inferred from the data. It is worth noting that for the AWC region, a wave energy peak is observed around 28 months, whereas the residual shoreline signal peaks at approximately 30 months. This indicates that the f^{peak} band is not always free of wave-energy variability. Such features may arise from the broad and irregular spectrum of ENSO-related forcing, which can interact with other climate modes (e.g., IOD or SAM in this region), giving rise to secondary or shifted spectral peaks through winds cascading on wave generation. Importantly, the high phase-coherence metric R_w obtained for AWC (Fig. 4c) indicates a robust phase relationship between shoreline and wave energy signals at the semi-annual timescale. Therefore, band-limited wave-energy forcing and phase resonance may be concomitant, with resonance primarily injecting energy into the frequency band, while the wave forcing contributes to organizing the phase and, to a lesser extent, the period of the shoreline oscillation. This interplay highlights the broad diversity of dynamical behaviors across global coastal environments.

3.3.2 Asymmetric annual wave forcing

We previously described a regional mechanism in which wave activity departs from a purely sinusoidal annual cycle, exhibiting a pronounced semi-annual component that produces multi-peaked patterns in wave energy. Such regions are mainly found along eastern boundary upwelling systems and across the Maritime Continent, where the timing or amplitude of local winds is shifted relative to the hemispheric winter maximum (Colosi et al., 2021) that generates long-period swells. This shift largely results from the seasonal reversal of the monsoon winds, which generates alternating peaks in wave height during the northwest and southeast monsoon periods (Purwanto et al., 2021). In turn, this semi-annual frequency in the wave forcing can interact nonlinearly with the intrinsic semi-annual timescales of shoreline adjustment, producing a resonant peak at periods of approximately 21–32 months.

Fig. 4.a,d reveals that the 21–32 months emergent timescales from triadic resonance in the SDS occur beyond regions where the previously describe mechanism occurs. Particularly, such emergent timescales are observed in semi-enclosed basins such as the eastern Mediterranean Sea or the Gulf of Mexico. Fig. 5 shows that, in these areas, wind-wave and swell activity share similar timing. For instance, in the Caribbean Sea, the Caribbean Low-Level Jet and the seasonal migration of the Intertropical Convergence Zone generate maximum wave energy in late summer–autumn, coinciding with the hurricane season that produces long-period swell (Morales-Márquez et al., 2023; Lemessy et al., 2021). Similar synchronous timing is observed in the Mediterranean Sea (Sartini et al., 2015; Flaounas et al., 2022). Yet, Fig. 7.a (which shows the amplitude ratio between the semi-annual (A_2) and annual (A_1) harmonics (A_2/A_1) of wave energy), reveals that the 6-month component still exerts a strong modulation of the wave-forcing cycle in these semi-enclosed regions. More surprisingly, these regions exhibit comparable (or even higher) rates of A_2/A_1 than eastern boundary upwelling systems, implying that a mechanism other than the phase shift

https://doi.org/10.5194/egusphere-2026-541
Preprint. Discussion started: 13 February 2026
© Author(s) 2026. CC BY 4.0 License.

between local wind-sea and remote swell can produce a semi-annual peak in wave forcing and trigger the observed triadic phase coupling.

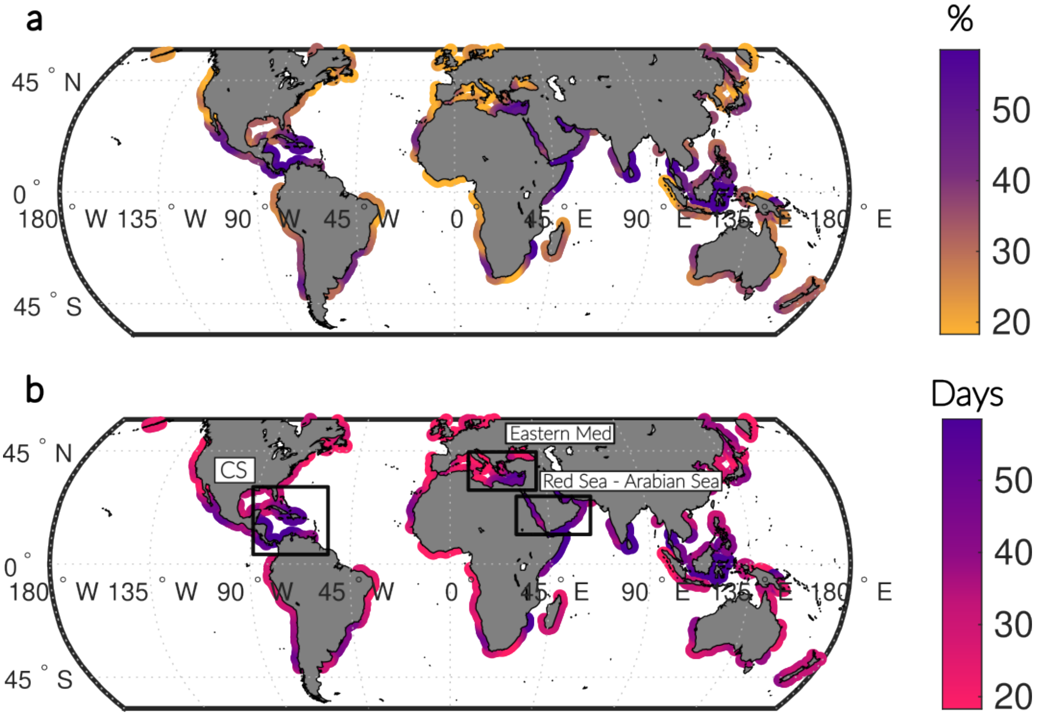

Figure 7. Amplitude ratio and temporal asymmetry of the annual wave cycle. (a) Ratio of the semi-annual to annual harmonic amplitudes (A_2/A_1, in %) of the climatological wave energy, illustrating the relative strength of the semi-annual component in the global wave-energy cycle. Elevated ratios ($>60\%$) identify regions where the semi-annual harmonic strongly modulates the annual cycle, particularly along tropical and subtropical coasts (e.g., Indonesia, Gulf of Guinea, Caribbean, and northwestern Australia). (b) Temporal asymmetry of the annual cycle, expressed as the number of days between the rising and falling crossings of the median climatological wave energy. Values near 0 days indicate a symmetric sinusoidal cycle, while shorter or longer intervals denote asymmetric cycles with faster rise or slower decay. The strongest asymmetries ($\geq$ 40–50 days) coincide spatially with the regions of enhanced semi-annual amplitude, confirming that temporal skewness in the seasonal wave forcing underlies the emergence of semi-annual variability and supports triadic resonance between the 6-month wave component and the shoreline response.

One possible candidate is the asymmetry of the annual wind-forcing cycle. Fig. 7.b illustrates this temporal asymmetry, expressed as the number of days separating the rising and falling crossings of the median annual cycle of wave energy, thereby providing a measure of the intraseasonal skewness of the seasonal forcing. Pronounced skewness is indeed observed in semi-enclosed seas such as the Caribbean, eastern Mediterranean, and Arabian Seas. This diagnostic is further supported by the cross-recurrence plots shown in Fig. 8, which explicitly compare the ascending (Jan–Jun) and descending (Jul–Dec) phases of the annual wave-energy cycle. Each panel shows the cross-recurrence matrix between these two semi-annual segments for three representative regions (black boxes in Fig. 7.b). In these matrices, a value of 1 indicates that the two phases exhibit similar daily mean wave-energy values at the corresponding calendar dates, whereas a value of 0 indicates dissimilarity. As a result, coherent light-blue bands falling along the red-dashed diagonal in Fig. 8 highlight portions of the year where the rising and falling limbs of the seasonal cycle are dynamically similar, while fragmented or curved patterns indicate strong asymmetry between the two regimes. This visualization therefore provides a direct, time-resolved view of the degree of semi-annual symmetry (or lack thereof) in wave forcing.

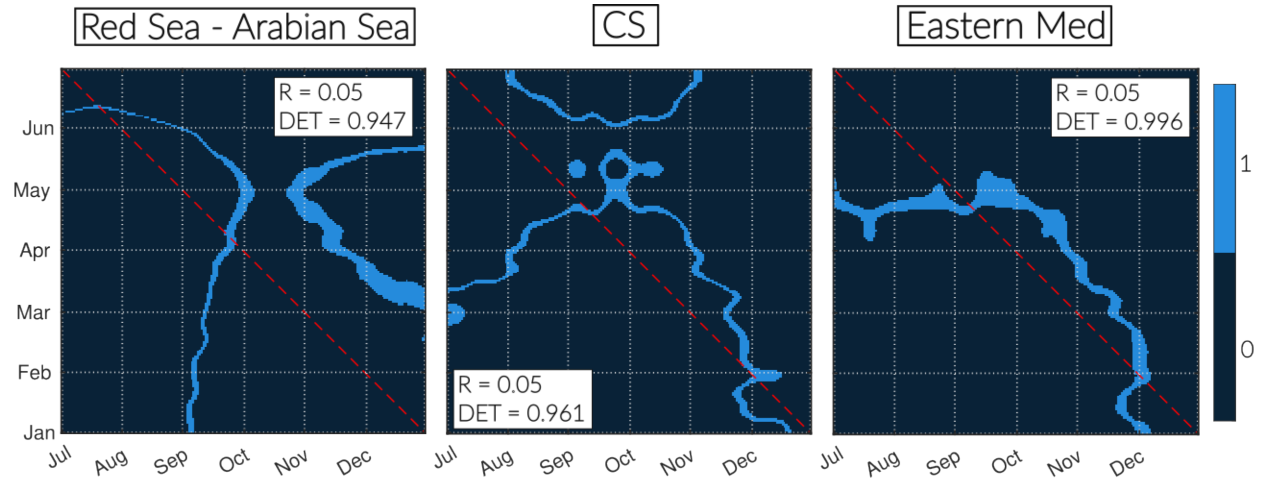

Figure 8. Cross-recurrence plots between the ascending (Jan–Jun) and descending (Jul–Dec) phases of the annual wave energy cycle in three regions: Red Sea–Arabian Sea, Central Sector (CS), and Eastern Mediterranean. Each plot represents the recurrence similarity between the two semi-annual phases, with color intensity indicating the degree of similarity (1 = true; 0 = false). The red dashed line marks the line of perfect symmetry. The curvature and displacement of the main recurrence ridge indicate seasonal asymmetry between the rising and falling phases. Values of recurrence rate (R) and determinism (DET) quantify the density and temporal organization of recurrent states, respectively. Despite low overall recurrence ($R \approx 0.05$), high determinism ($DET > 0.94$) reveals a structured and consistent seasonal relationship, highlighting a stable coupling between the two halves of the annual energy cycle.

From these matrices, two standard recurrence quantification analysis indices were derived: the Recurrence Rate (RR) and the Determinism (DET) (Eckmann et al., 1995; Martins et al., 2017). The recurrence rate:

$$RR = \frac{1}{N^2}\sum_{i,j} R_{ij}, \tag{14}$$

measures the overall density of recurrent states, i.e., the proportion of days for which the wave energy during the ascending phase matches that during the descending phase within a fixed tolerance (here the 5^{th} percentile of all distances). The determinism:

$$DET = \frac{\sum_{l \geq l_{\min}} l\,P(l)}{\sum_{i,j} R_{ij}}, \tag{15}$$

quantifies the proportion of recurrent points forming diagonal lines, reflecting the temporal organization of similar dynamical patterns. Low RR values (≈ 0.05) indicate that direct correspondences between the two halves of the seasonal cycle are rare,

https://doi.org/10.5194/egusphere-2026-541
Preprint. Discussion started: 13 February 2026
© Author(s) 2026. CC BY 4.0 License.

whereas high DET values (> 0.94) reveal that when such similarities occur, they are temporally coherent and structured. This combination highlights a nonlinear yet stable seasonal coupling, where the evolution of wave energy follows a consistent but asymmetric trajectory between the growth and decay phases of the annual cycle. Regionally, the cross-recurrent plots reveal contrasted behaviors among the main basins. The Red Sea–Arabian Sea and Caribbean Sea (CS) exhibit strong semi-annual recurrence structures, consistent with the pronounced A_2/A_1 ratios identified in Fig. 7.a. In these basins, the recurrence ridges are highly curved and sometimes duplicated, indicating that the semi-annual peak is itself asymmetric between the rising and falling phases. Conversely, the Eastern Mediterranean displays no significant semi-annual peak, reflecting a predominantly asymmetric annual cycle with limited semi-annual modulation.

Both diagnostics (Fig. 7.b and Fig. 8) consistently highlight the same set of regions (eastern Mediterranean Sea, Indonesia, Red Sea, Arabian Sea, and parts of the Caribbean), where the strong semi-annual-to-annual ratio is not driven by a phase shift between wind-sea and swell, but due to the intraseasonal asymmetry of the wave-energy cycle. This second mechanism explains the elevated R_w values observed in these areas (Fig. 4.d); revealing that semi-annual forcing can emerge from two distinct physical processes.

4 Discussion

This study provides robust evidence that a substantial fraction of shoreline variability at interannual timescales cannot be explained within a purely linear forcing–response framework. The emergence of a quasi-biennial (≈20–30 months) shoreline mode (recurrent across disparate coastal environments), instead points to a nonlinear mechanism intrinsic to the coupled wave–shoreline system. The identification of a triadic resonance linking near semi-annual wave forcing, and lagged (semi-annual) shoreline response, and an emergent low-frequency shoreline signal establishes nonlinear phase coupling as a meaningful candidate in shaping part of shoreline variability. This suggests that shorelines can act as a nonlinear integrator, redistributing energy across frequencies through delayed and phase-locked interactions.

The proposed resonance mechanism is supported by three independent and converging lines of evidence. First, the near-biennial frequency is detected after the linear contribution of known environmental forcings is removed, and is absent from the forcing spectra themselves. Second, the phase coherence analysis demonstrates statistically significant and energetically weighted phase locking between the three interacting components, ruling out spurious spectral coincidences. Third, the same interaction is independently observed in long-term *in situ* measurements at Torrey Pines, confirming that the signal is not an artifact of satellite processing, spatial aggregation, or methodological bias. Importantly, the resonance does not require continuous excitation. Rather, intermittent but recurrent phase coupling episodes are sufficient to sustain the emergent mode over multi-decadal records. This behavior is consistent with the response of weakly nonlinear, dissipative systems subject to temporally modulated forcing, where resonance can be activated episodically yet leave a persistent spectral imprint (Tomita, 2014).

To further assess the physical plausibility of the proposed triadic mechanism, we implemented a minimal forced–oscillator model driven by the product of two observed semi-annual signals : the wave-energy band (x_1) and the corresponding semi-

https://doi.org/10.5194/egusphere-2026-541
Preprint. Discussion started: 13 February 2026
© Author(s) 2026. CC BY 4.0 License.

annual shoreline response (x_2). The model is intentionally simple and does not aim to reproduce the full shoreline dynamics. Instead, it serves as a conceptual framework to disentangle the respective roles of nonlinear energy injection and intrinsic shoreline dynamics in the emergence of near-biennial variability.

The modeled shoreline response $y(t)$ is governed by a damped linear oscillator forced by the nonlinear interaction term:

$$\frac{\mathrm{d}^2 y}{\mathrm{d}t^2} + \lambda \frac{\mathrm{d}y}{\mathrm{d}t} + \omega_0^2 y = \alpha x_1(t) x_2(t), \tag{16}$$

where λ is a linear damping coefficient, $\omega_0 = 2\pi/T_0$ is the intrinsic angular frequency of the oscillator, and α controls the strength of the forcing. The multiplicative term $x_1(t)x_2(t)$ explicitly represents the nonlinear coupling between the semi-annual components of wave forcing and lagged shoreline response. Importantly, the signals used here are time-series taken in the satellite-derived dataset for a random location where $R_w > 0.5$. Moreover, no interannual frequency is prescribed in either the forcing or the intrinsic dynamics of the model.

The time–frequency analysis of the simulated shoreline response, averaged over a wide range of intrinsic periods ($T_0 =$ 5:1:35 months), reveals a persistent interannual energy band between 20 and 30 months (Fig. 9a). A similar band is observed in the wavelet spectrum of the nonlinear forcing term x_1x_2 (Fig. 9b). The close correspondence between these two panels demonstrates that the near-biennial frequency is already embedded in the nonlinear interaction between the two semi-annual components, rather than arising from the intrinsic dynamics of the oscillator. This provides a direct, signal-based demonstration of the physical plausibility of the proposed resonance mechanism. In other words, the triadic interaction injects energy into the near-biennial band independently of the shoreline adjustment timescale. Moreover, beach systems are known to exhibit memory and self-adjusting timescales in response to external forcing (Davidson et al., 2013). As such, the role of the system's intrinsic dynamics is also of interest. Here, this role is examined by analyzing how the energy injected through triadic resonance is processed by the modeled shoreline system. Figure 9c shows the mean energy contained within the 18–35 month band of the simulated response as a function of the intrinsic period T_0 and the damping coefficient λ. Enhanced interannual energy emerges only over a restricted region of the parameter space, where the intrinsic adjustment timescale overlaps with the interannual band and dissipation remains sufficiently weak. This demonstrates the conditional nature of the resonance: nonlinear energy injection alone may not be sufficient to sustain a strong and persistent interannual signal. This behavior is further quantified using a frequency-dependent gain analysis (Fig. 9d,e). The gain is defined as:

$$G(f) = \frac{P_y(f)}{P_{x_1x_2}(f)} \tag{17}$$

where $P_y(f)$ denotes the power spectral density of the simulated system response, and $P_{x_1x_2}(f)$ corresponds to the power spectral density of the nonlinear forcing term resulting from the triadic interaction between the two semi-annual components. The gain thus measures the frequency-dependent sensitivity of the system to nonlinear forcing, independently of the forcing amplitude. Evidently, while the location of the interannual gain peak remains largely invariant across intrinsic periods, its amplitude and sharpness depend strongly on the intrinsic period T_0 for a given damping coefficient λ (Fig. 9d).

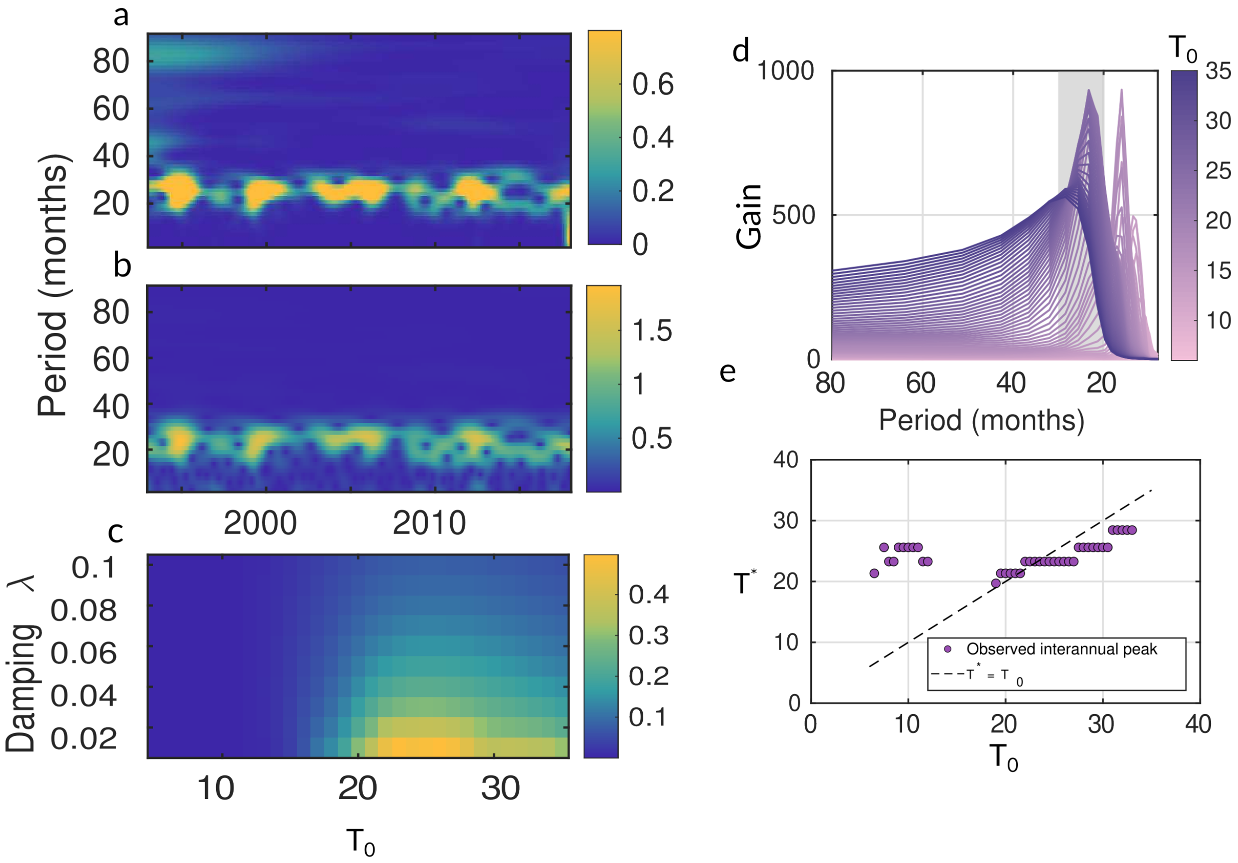

Figure 9. Dynamical interpretation of the triadic resonance mechanism using a minimal forced–oscillator model. (a) Time–frequency representation (wavelet power spectrum) of the simulated shoreline response $y(t)$, averaged over a wide range of intrinsic periods ($T_0 = 2$–35 months). Despite variations in the intrinsic dynamics, a persistent energy band emerges in the interannual range (20–30 months). (b) Wavelet power spectrum of the nonlinear forcing term x_1x_2, showing a similar interannual energy band. The close correspondence between panels (a) and (b) indicates that the near-biennial frequency is injected by the nonlinear interaction between the two semi-annual components. (c) Mean interannual energy of the simulated response as a function of intrinsic period T_0 and damping coefficient λ. Enhanced energy is observed when the intrinsic adjustment timescale overlaps with the interannual band and damping is weak, highlighting the conditional nature of the resonance. (d) Frequency-dependent gain $G(f) = P_y(f)/P_{x_1x_2}(f)$ for a range of intrinsic periods T_0 (color-coded). While the location of the interannual gain peak remains stable across T_0, its amplitude and sharpness depend on the intrinsic dynamics, with maximum amplification occurring when T_0 lies within the interannual range. (e) Period of maximum gain T^* within the interannual band as a function of intrinsic period T_0. The dashed line indicates $T^* = T_0$. For small T_0, the response is forcing-dominated and weakly organized. As T_0 approaches the interannual band, a locking regime emerges in which the intrinsic mode and the triadically generated frequency overlap, leading to enhanced coherence. For larger T_0, the response becomes independent of the intrinsic timescale, indicating a permissive regime in which the intrinsic dynamics allow the injected interannual energy to persist without controlling its frequency. To avoid spurious detections, T^* is retained only when the interannual gain maximum corresponds to an interior spectral peak within the target band, excluding cases where the maximum occurs at the edges of the band and may reflect truncation or boundary effects rather than a physically meaningful response.

Moreover, Fig. 9e depicts the evolution of the period of maximum gain within the 18–35 month band (T^*) as a function of the intrinsic period T_0. For short intrinsic periods, the response to interannual forcing is weak and spectrally diffuse (pink point far from the diagonal). As T_0 approaches the interannual range, a locking regime emerges in which the intrinsic mode and the triadically generated frequency band overlap, leading to enhanced amplification and spectral coherence. For larger intrinsic periods, the response becomes only weakly dependent on T_0, indicating a permissive regime in which the intrinsic dynamics no longer constrain frequency selection but allow the injected interannual energy to persist.

These results indicate that nonlinear resonance alone is sufficient to inject energy into the interannual band, but may be insufficient to produce a coherent oscillatory mode through long time intervals. A compatible intrinsic adjustment timescale may be required to organize this energy into a persistent and observable signal. In this sense, the intrinsic modeled shoreline dynamics act as a frequency-selective filter that controls the expression, rather than the existence, of the emergent near-biennial variability; raising the question of the potential role and existence of an internal beach mode in structuring the nonlinear energy injection into the system as those lacking such an internal timescale would still experience nonlinear energy injection at interannual periods, but only as weak and intermittent fluctuations rather than as a dominant oscillatory component.

The consistency between this conceptual model, the regional analyses, the global satellite observations, and independent *in situ* measurements strengthens the physical basis of the triadic resonance mechanism proposed in this study. Repeating the same idealized-model experiments for different locations with $R_w \geq 0.5$ (i.e. different $x_1(t)$ and $x_2(t)$) leads to quantitatively different amplitudes but does not alter the qualitative behavior of the system, indicating that the emergence of the interannual band and its dependence on intrinsic timescales are robust features of the triadic mechanism rather than site-specific artifacts.

A central outcome of this work is the identification of semi-annual variability as a key gateway for nonlinear energy transfer in coastal systems. We show that semi-annual wave forcing arises from two distinct but widespread mechanisms: (i) phase opposition between locally generated wind–sea and remotely generated swell along eastern boundary systems, and (ii) temporal asymmetry of the annual wind–wave cycle in monsoonal and semi-enclosed basins. Despite their different origins, both mechanisms introduce a robust 6-month harmonic in wave energy able to inject energy within the shoreline. The interaction between these two semi-annual oscillations (forcing and lagged response), creates the conditions required for triadic resonance and the subsequent emergence of a lower-frequency shoreline mode.

These implications are consistent with recent findings showing that allowing model parameters to vary in time does not necessarily improve shoreline predictions when baseline equilibrium models are already well calibrated, except during periods of extreme forcing or regime shifts (Azorakos et al., 2025). In such cases, parameter variability has been shown to act primarily as an adaptive mechanism that compensates for unresolved dynamics rather than as a direct physical response to wave energy alone. This suggests that nonlinear interactions, mediated by the system's intrinsic memory and its ability to integrate forcing over time, play a central role in modulating shoreline variability. From a predictive standpoint, this implies that shoreline forecasts based solely on linear correlations with wave energy or sea level may systematically underestimate variability at intermediate timescales, even when augmented with data assimilation. Incorporating nonlinear phase interactions and resonance mechanisms into reduced-order shoreline models could therefore provide a more physically grounded alterna-

https://doi.org/10.5194/egusphere-2026-541
Preprint. Discussion started: 13 February 2026
© Author(s) 2026. CC BY 4.0 License.

tive to time-varying free parameters, improving model realism and predictive skill, particularly in regions identified here as resonance-prone and exposed to complex or evolving wave climates.

More broadly, this study positions sandy shorelines alongside other geophysical systems in which emergent modes arise from nonlinear interactions rather than direct forcing. The triadic resonance identified here is conceptually analogous to combination tones in acoustics or to climate–seasonal cycle interactions in the tropical ocean–atmosphere system. Recognizing such mechanisms in coastal morphodynamics opens new avenues for interpreting unexplained interannual variability reported in previous field studies and highlights the need to revisit shoreline dynamics from a nonlinear systems perspective.

5 Limitations

Despite the robustness of the triadic resonance signal identified here, several limitations must be acknowledged.

First, the analysis relies on satellite-derived shoreline positions aggregated at regional scales. While this aggregation is necessary to suppress noise and reveal coherent dynamics, it inevitably smooths local processes such as alongshore gradients, transient sediment pathways, or site-specific morphodynamic feedbacks. As a result, the mechanism identified here should be interpreted as a regional-scale dynamical tendency.

Second, the residual shoreline signal is obtained after iterative removal of linear contributions from a predefined set of forcings using an iterative EOF approach. Although extensive sensitivity tests and synthetic-noise experiments indicate that this procedure does not introduce artificial frequencies, it cannot fully exclude the influence of unresolved or imperfectly represented forcings, nor subtle nonlinear effects that project weakly onto the retained modes.

Third, the triadic phase-coupling analysis detects intermittent and conditionally activated resonance, not a continuously operating mechanism. The observed near-biennial mode does not imply a permanent internal oscillation of the shoreline system, but rather the cumulative imprint of repeated phase-locked episodes over multi-decadal records. Consequently, the amplitude and temporal persistence of the signal vary substantially across regions and time periods.

Finally, the study focuses on microtidal sandy coasts and monthly temporal resolution. Extrapolation to macrotidal environments, gravel beaches, or systems dominated by episodic extremes should be made with caution. Higher-frequency observations and site-specific morphodynamic data will be required to assess how this nonlinear mechanism interacts with event-scale processes and long-term shoreline trends.

6 Conclusion

This study demonstrates that a significant fraction of interannual shoreline variability can emerge from nonlinear interactions within the coupled shoreline–wave system, rather than being directly inherited from external forcings acting at the same timescale. Using satellite-derived shoreline observations at the global scale, supported by long-term *in situ* measurements, we identify a recurrent near-biennial shoreline signal (approximately 20–30 months) that is absent from the dominant frequencies of known forcings.

Through amplitude-weighted triadic phase coherence analysis, we show that this variability arises from a nonlinear interaction between semi-annual wave-energy fluctuations and a lagged semi-annual shoreline response. The resulting triadic resonance generates a low-frequency shoreline mode that is spatially coherent across multiple eastern boundary systems and semi-enclosed basins. A minimal forced-oscillator experiment further confirms that such a timescale can emerge naturally from the nonlinear coupling between these two semi-annual components, without prescribing any interannual forcing.

Together, these results highlight nonlinear phase coupling as a key mechanism shaping shoreline variability at interannual timescales. They suggest that shorelines cannot be fully understood as linear responders to external forcing, but instead behave as nonlinear systems capable of redistributing energy across frequencies through delayed interactions.

Several limitations should be acknowledged. First, the satellite-derived shoreline record, while spatially extensive and multi-decadal, remains constrained by temporal resolution and measurement uncertainty, which may limit the detectability of higher-frequency nonlinear interactions. Second, the forced-oscillator model employed here is intentionally idealized and does not aim to reproduce the full complexity of coastal morphodynamics; rather, it serves to demonstrate dynamical plausibility. As such, it does not account for alongshore sediment transport, three-dimensional morphodynamics, or feedbacks with tides and sea level.

In addition, the resonance mechanism identified here is not continuously active, but occurs intermittently when phase and energy conditions are favorable. Understanding the controls on the timing, duration, and spatial extent of these resonant episodes remains an open question. Future work should therefore focus on integrating nonlinear interaction diagnostics into process-based shoreline models and exploring how projected changes in wave climate, storm seasonality, and swell propagation may alter resonance-prone regions.

By explicitly accounting for nonlinear interactions between shoreline response and wave forcing, this study opens new perspectives for interpreting unexplained interannual shoreline variability and for improving the physical realism of large-scale shoreline projections under changing climate conditions.

Code availability. Matlab codes and processed data are made available upon request.

Data availability. Global satellite-derived sandy shoreline can be found at: Global Satellite Dataset.

The ERA-5 wave dataset is available at: Copernicus ERA5 dataset

Torrey Pines Beach *in situ* dataset is available at: Torrey Pines Beach dataset

Author contributions. R.A., J.B., L.L., and M.A. wrote and proofread the manuscript. All authors contributed to the scientific work and discussion. All authors reviewed the manuscript.

© Author(s) 2026. CC BY 4.0 License.

Competing interests. The authors declare no competing interest.

Financial support. This study has been partially supported through the grant EUR TESS N°ANR-18-EURE-0018 in the framework of the Programme des Investissements d'Avenir.

Appendix A: Signal reconstruction and robustness assessment

Wave forcing and SLA have both been identified as primary drivers of shoreline variability over large coastal regions (Almar et al., 2023). However, in the present analysis we focused on wave forcing, as it was the only driver exhibiting a strong and consistent semi-annual frequency capable of exciting shoreline change at the frequencies suspected to produce the observed triadic resonance (Fig. A1), consistent with the shoreline residual frequency f ($T \approx 21$–32 months) shown in Fig 3.a.

Therefore, to assess phase coherence between shoreline signals $S_i(t)$ and wave energy signals $E_{w_i}(t)$, and thereby evaluate the resonance hypothesis, we analyzed their temporal variability using the continuous wavelet transform (CWT) with a Morse wavelet (Torrence and Compo, 1998). The CWT provides a joint time–frequency representation,

$$W_x(f,\tau) = \int_{-\infty}^{+\infty} x(t)\,\psi^*_{f,\tau}(t)\,dt, \tag{A1}$$

where $\psi_{f,\tau}(t)$ is the wavelet function centered at time τ and scaled according to frequency f. The Morse wavelet was chosen for its good frequency localization and robustness for finite-length, nonstationary signals (Hubbard, 1998). Before analysis, all series were symmetrically padded (50 points) to mitigate boundary effects. Wavelet derived frequency-domain results were further cross-checked using complementary fast Fourier transform (FFT) analyses.

To focus on the sub-annual band of interest, all coefficients corresponding to periods longer than 7 months were set to zero,

$$W_x^{\text{filt}}(f,\tau) = \begin{cases} W_x(f,\tau), & T = 1/f < 7 \text{ months},\\ 0, & \text{otherwise,} \end{cases} \tag{A2}$$

and the filtered signal was reconstructed by inverse wavelet transform,

$$x^{\text{filt}}(t) = \mathcal{W}^{-1}\big(W_x^{\text{filt}}(f,\tau)\big). \tag{A3}$$

This filtering isolates high-frequency oscillations, potentially associated with resonance, while excluding seasonal or longer-term variability (Fig. A2a-b, A2d-g).

For each location, we quantified the relative importance of these modes using the energy ratio,

$$R_i^{(S)} = \frac{\sum |W_{S_i}^{\text{filt}}|^2}{\sum |W_{S_i}|^2}, \qquad R_i^{(E_w)} = \frac{\sum |W_{E_{w_i}}^{\text{filt}}|^2}{\sum |W_{E_{w_i}}|^2}, \tag{A4}$$

© Author(s) 2026. CC BY 4.0 License.

which expresses the fraction of total variance carried by sub-annual periods. To complement this, we estimated the persistence duration D_i as the cumulative length of contiguous intervals defined as

$$D_i^{(S)} = \sum_k \Delta t_k^{(S)}, \qquad D_i^{(E_w)} = \sum_k \Delta t_k^{(E_w)}, \tag{A5}$$

where each Δt_k corresponds to the duration of a time interval during which the band-limited wavelet power exceeds the mean power of the original signal. This metric therefore measures the cumulative persistence of energetic sub-annual oscillations throughout the record. This dual characterization captures both the strength and the temporal consistency of the targeted oscillations to ensure significance with regard to the original signals.

Because shoreline response may be lagged with respect to wave forcing, we also evaluated their frequency-specific coupling via magnitude-squared coherence,

$$C_{SE_w}(f) = \frac{|P_{SE_w}(f)|^2}{P_{SS}(f)\,P_{E_wE_w}(f)}, \tag{A6}$$

where $P_{SE_w}(f)$ is the cross-spectral density and $P_{SS}(f)$, $P_{E_wE_w}(f)$ the auto-spectra. We focused on the 5–7 month band (Fig. A2f, A2g), where resonance-like modes were hypothesized (Fig. A1), and retained the maximum coherence value together with its associated period.

Statistical significance was assessed against the critical threshold

$$C_{\text{crit}} = 1 - \varepsilon^{1/(L-1)}, \tag{A7}$$

with $\varepsilon = 0.05$ (95% confidence) and L the number of independent spectral segments (Jenkins and Watts, 1969). In practice, L depends on the Welch parameters used for coherence estimation. We selected a window size of 64 months (approximately 5 years) with 50% overlap (32 months), which provides a compromise between spectral resolution and the number of segments available in our 25-year (n = 301 months) records. This yields about $L \approx n/(64-32) \simeq 9$ independent averages, ensuring that coherence estimates are based on multiple realizations. Only sites with $C_{SE_w}^{\max} \geq C_{\text{crit}}$ were retained, ensuring that the detected relationships were statistically robust rather than spurious (Fig. A2.c).

To synthesize the indicators, each metric was normalized using a z-score,

$$z(x) = \frac{x - \mu(x)}{\sigma(x)}, \tag{A8}$$

and combined into composite scores. For shoreline variability,

$$Sc_i^{(S)} = \alpha\, z(R_i^{(S)}) + \beta\, z(D_i^{(S)}), \tag{A9}$$

and for wave energy,

$$Sc_i^{(E_w)} = \alpha\, z(R_i^{(E_w)}) + \beta\, z(D_i^{(E_w)}), \tag{A10}$$

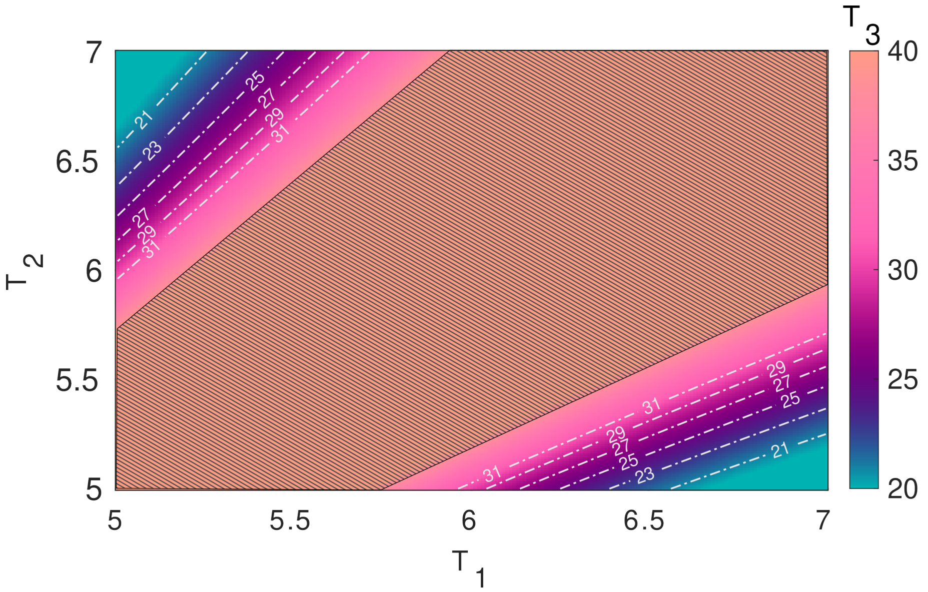

Figure A1. Combination map of two input periods T_1 and T_2 (in months). The background color represents the resulting interaction period $T_3 = 1/|f_1 - f_2|$, where $f_1 = 1/T_1$ and $f_2 = 1/T_2$. The dashed patch corresponds to cases where $|f_1 - f_2| \rightarrow 0$ (i.e., $T_3 \rightarrow \infty$), as it approach the diagonal. White doted-dashed lines indicate the admissible combinations of (T_1, T_2), sampled at 5 x 10^{-2}-month resolution, that fall within the observed range of T_3^{obs} (10th–90th percentiles resulting from Shoreline residual (S'_{res}) signal spectral analysis (Fig. 3.d)).

with equal weights $\alpha = \beta = 0.5$. Here, no metric (either R or D) was favoured, as we found no rational, evidence-backed justification to support one over the other. Finally, the joint indicator was defined as

$$Sc_i^{\text{joint}} = \frac{1}{2}\left(Sc_i^{(S)} + Sc_i^{(E_w)}\right), \tag{A11}$$

providing a balanced measure of variance contribution, persistence, and shoreline–wave coherence. To retain only robust cases, the lowest 15% of joint scores were discarded.

Together, these steps (including wavelet filtering, energy and persistence analysis, coherence testing and composite scoring), ensure that the reconstructed signals capture genuine sub-annual variability in shoreline dynamics and wave forcing, rather than artifacts of seasonality or noise (Fig. A2.c).

© Author(s) 2026. CC BY 4.0 License.

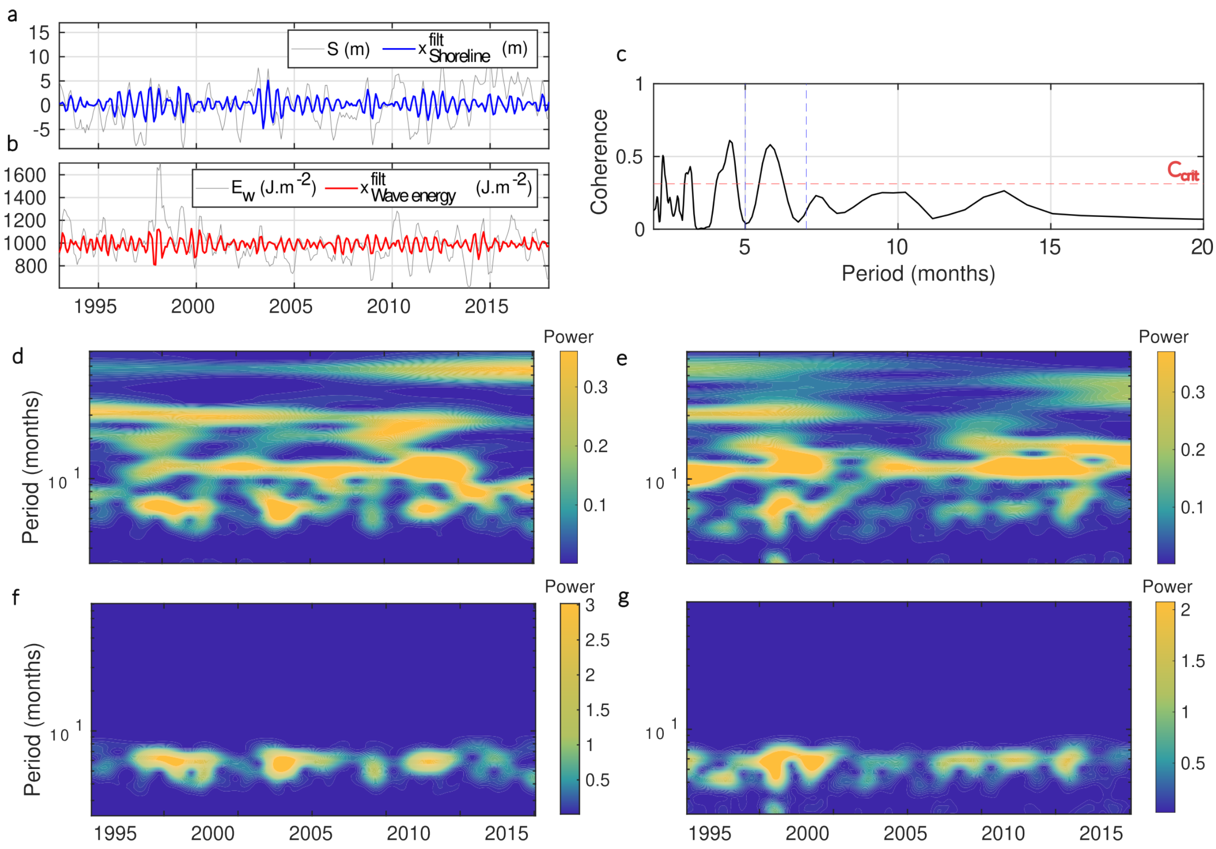

Figure A2. Illustration of the shoreline and wave signal reconstruction and robustness assessment. (a–b) Original shoreline (S) and wave energy (E_w) signals (gray) and their reconstructed high-frequency components (T < 7 months) via a wavelet transform (blue, red). (c) Magnitude-squared coherence between the normalized versions of $x^{filt}_{shoreline}$ and $x^{filt}_{Wave\ energy}$. The blue dashed lines indicate the period of interest where resonance is expected (5–7 months), and the red dashed line shows the critical coherence level (C_{crit}). (d–e) Wavelet spectra of the original shoreline (d) and wave energy (e) normalized signals. (f–g) Same but for the high-frequency reconstructed and normalized signals for shoreline (f) and wave energy (g). The location shown here has passed the joint score test, indicating that both shoreline and wave energy exhibit a significant semi-annual phased frequency band, which is successfully reconstructed by the wavelet transform. For visual clarity, the color scale limits have been adjusted independently to enhance feature visibility.

References

Almar, R., Boucharel, J., Graffin, M., Abessolo, G. O., Thoumyre, G., Papa, F., Ranasinghe, R., Montano, J., Bergsma, E. W. J., Baba, M. W., and Jin, F.-F.: Influence of El Niño on the variability of global shoreline position, Nature Communications, 14, 3133, https://doi.org/10.1038/s41467-023-38742-9, 2023.

Amman, O. H., von Kármán, T., and Woodruff, G. B.: The failure of the Tacoma Narrows Bridge, 1941.

Aubrey, D. G., Inman, D. L., and Nordstrom, C. E.: Beach profiles at Torrey Pines, California, Coastal Engineering Proceedings, pp. 75–75, 1976.

Azorakos, G., Castelle, B., Idier, D., Marieu, V., Ibaceta, R., Splinter, K. D., Bertin, S., Masselink, G., and Scott, T.: Investigating the potential of time-varying free parameters in equilibrium shoreline change models through data assimilation, Earth Surface Processes and Landforms, 50, e70 221, https://doi.org/https://doi.org/10.1002/esp.70221, 2025.

Banno, M., Nakamura, S., Kosako, T., Nakagawa, Y., Yanagishima, S.-i., and Kuriyama, Y.: Long-term observations of beach variability at Hasaki, Japan, Journal of Marine Science and Engineering, 8, 871, 2020.

Barral, J. and Martin, P.: Phantom tones and suppressive masking by active nonlinear oscillation of the hair-cell bundle, Proceedings of the National Academy of Sciences, 109, E1344–E1351, https://doi.org/10.1073/pnas.1202426109, 2012.

Bergsma, E. W. J., Klotz, A. N., Artigues, S., Graffin, M., Prenowitz, A., Delvit, J.-M., and Almar, R.: Shoreliner: A Sub-Pixel Coastal Waterline Extraction Pipeline for Multi-Spectral Satellite Optical Imagery, Remote Sensing, 16, 2795, https://doi.org/10.3390/rs16152795, 2024.

Boucharel, J. and Jin, F.-F.: A simple theory for the modulation of tropical instability waves by ENSO and the annual cycle, Tellus A: Dynamic Meteorology and Oceanography, 72, 1700 087, https://doi.org/10.1080/16000870.2019.1700087, 2020.

Boucharel, J., Timmermann, A., and Jin, F.-F.: Zonal phase propagation of ENSO sea surface temperature anomalies: Revisited, Geophysical Research Letters, 40, 4048–4053, 2013.

Boucharel, J., Almar, R., Kestenare, E., and Jin, F.-F.: On the influence of ENSO complexity on Pan-Pacific coastal wave extremes, Proceedings of the National Academy of Sciences, 118, e2115599 118, 2021.

Brown, E. W.: Elements of the Theory of Resonance: Illustrated by the Motion of a Pendulum, vol. 19, Cambridge University Press, 2011.

Burkett, V. R., Wilcox, D. A., Stottlemyer, R., Barrow, W., Fagre, D., Baron, J., Price, J., Nielsen, J. L., Allen, C. D., Peterson, D. L., Ruggerone, G., and Doyle, T.: Nonlinear dynamics in ecosystem response to climatic change: Case studies and policy implications, Ecological Complexity, 2, 357–394, https://doi.org/https://doi.org/10.1016/j.ecocom.2005.04.010, 2005.

Carrere, L., Lyard, F., Cancet, M., Allain, D., Dabat, M.-L., Fouchet, E., Sahuc, E., Faugere, Y., Dibarboure, G., and Picot, N.: A new barotropic tide model for global ocean: FES2022, in: 2022 Ocean Surface Topography Science Team Meeting, p. 43, 2022.

Castelle, B., Kras, E., Masselink, G., Scott, T., Konstantinou, A., and Luijendijk, A.: Satellite-derived sandy shoreline trends and interannual variability along the Atlantic coast of Europe, preprint, In Review, https://doi.org/10.21203/rs.3.rs-3696677/v1, 2023.

Colosi, L. V., Villas Bôas, A. B., and Gille, S. T.: The Seasonal Cycle of Significant Wave Height in the Ocean: Local Versus Remote Forcing, Journal of Geophysical Research: Oceans, 126, e2021JC017 198, https://doi.org/10.1029/2021JC017198, 2021.

Davidson, M., Splinter, K., and Turner, I.: A simple equilibrium model for predicting shoreline change, Coastal Engineering, 73, 191–202, https://doi.org/10.1016/j.coastaleng.2012.11.002, 2013.

Decharme, B., Delire, C., Minvielle, M., Colin, J., Vergnes, J.-P., Alias, A., Saint-Martin, D., Séférian, R., Sénési, S., and Voldoire, A.: Recent Changes in the ISBA-CTRIP Land Surface System for Use in the CNRM-CM6 Climate Model and in Global Off-Line Hydrological Applications, Journal of Advances in Modeling Earth Systems, 11, 1207–1252, https://doi.org/10.1029/2018MS001545, 2019.

Dee, D. P., Uppala, S. M., Simmons, A. J., Berrisford, P., Poli, P., Kobayashi, S., Andrae, U., Balmaseda, M. A., Balsamo, G., Bauer, P., Bechtold, P., Beljaars, A. C. M., van de Berg, L., Bidlot, J., Bormann, N., Delsol, C., Dragani, R., Fuentes, M., Geer, A. J., Haimberger, L., Healy, S. B., Hersbach, H., Hólm, E. V., Isaksen, L., Kållberg, P., Köhler, M., Matricardi, M., McNally, A. P., Monge-Sanz, B. M., Morcrette, J.-J., Park, B.-K., Peubey, C., de Rosnay, P., Tavolato, C., Thépaut, J.-N., and Vitart, F.: The ERA-Interim reanalysis: configuration and performance of the data assimilation system, Quarterly Journal of the Royal Meteorological Society, 137, 553–597, https://doi.org/https://doi.org/10.1002/qj.828, 2011.

Echevarria, E. R., Hemer, M. A., and Holbrook, N. J.: Seasonal Variability of the Global Spectral Wind Wave Climate, Journal of Geophysical Research: Oceans, 124, 2924–2939, https://doi.org/10.1029/2018JC014620, 2019.

Eckmann, J.-P., Kamphorst, S. O., and Ruelle, D.: Recurrence plots of dynamical systems, in: Turbulence, strange attractors and chaos, pp. 441–445, World Scientific, 1995.

Flaounas, E., Davolio, S., Raveh-Rubin, S., Pantillon, F., Miglietta, M. M., Gaertner, M. A., Hatzaki, M., Homar, V., Khodayar, S., Korres, G., Kotroni, V., Kushta, J., Reale, M., and Ricard, D.: Mediterranean cyclones: current knowledge and open questions on dynamics, prediction, climatology and impacts, Weather and Climate Dynamics, 3, 173–208, https://doi.org/10.5194/wcd-3-173-2022, 2022.

García-Reyes, M., Lamont, T., Sydeman, W. J., Black, B. A., Rykaczewski, R. R., Thompson, S. A., and Bograd, S. J.: A comparison of modes of upwelling-favorable wind variability in the Benguela and California current ecosystems, Journal of Marine Systems, 188, 17–26, https://doi.org/https://doi.org/10.1016/j.jmarsys.2017.06.002, benguela: Opportunity, Challenge and Change, 2018.

Graffin, M., Almar, R., Bergsma, E. W. J., Boucharel, J., Vitousek, S., Taherkhani, M., and Ruggiero, P.: Waterline responses to climate forcing along the North American West Coast, Communications Earth & Environment, 6, 444, https://doi.org/10.1038/s43247-025-02414-x, 2025a.

Graffin, M., Touzé, T., Bergsma, E. W., and Almar, R.: Towards a global assessment of sandy shorelines: Systematic extraction and validation of optical satellite-derived coastal indicators at various sites, Remote Sensing of Environment, 331, 115 033, 2025b.

Grinsted, A., Moore, J. C., and Jevrejeva, S.: Application of the cross wavelet transform and wavelet coherence to geophysical time series, Nonlinear Processes in Geophysics, 11, 561–566, https://doi.org/10.5194/npg-11-561-2004, 2004.

Hannachi, A.: A primer for EOF analysis of climate data, Department of Meteorology, University of Reading, 1, 3, 2004.

Hersbach, H.: ERA5 hourly data on single levels from 1940 to present. Copernicus Climate Change Service (C3S) Climate Data Store (CDS), 2018.

Hubbard, B. B.: The world according to wavelets: the story of a mathematical technique in the making, AK Peters/CRC Press, 1998.

Hulskamp, R., Luijendijk, A., Van Maren, B., Moreno-Rodenas, A., Calkoen, F., Kras, E., Lhermitte, S., and Aarninkhof, S.: Global distribution and dynamics of muddy coasts, Nature Communications, 14, 8259, https://doi.org/10.1038/s41467-023-43819-6, 2023.

Hurrell, J. W.: Decadal Trends in the North Atlantic Oscillation: Regional Temperatures and Precipitation, Science, 269, 676–679, https://doi.org/10.1126/science.269.5224.676, 1995.

Jenkins, G. M. and Watts, D. G.: Spectral analysis and its applications, Holden-Day Series in Time Series Analysis, 1969.

Jiang, F., Zhang, W., Boucharel, J., and Jin, F.-F.: Tropical origins of the Pacific Meridional Mode associated with the nonlinear interaction of ENSO with the annual cycle, Geophysical Research Letters, 50, e2023GL106 225, 2023.

© Author(s) 2026. CC BY 4.0 License.

Jin, F.-F., Neelin, J. D., and Ghil, M.: El Niño on the Devil's Staircase: Annual Subharmonic Steps to Chaos, Science, 264, 70–72, https://doi.org/10.1126/science.264.5155.70, 1994.

Konstantinou, A., Scott, T., Masselink, G., Stokes, K., Conley, D., and Castelle, B.: Satellite-based shoreline detection along high-energy macrotidal coasts and influence of beach state, Marine Geology, 462, 107 082, https://doi.org/10.1016/j.margeo.2023.107082, 2023.

Kroese, D. P. and Rubinstein, R. Y.: Monte Carlo methods, WIREs Computational Statistics, 4, 48–58, https://doi.org/https://doi.org/10.1002/wics.194, 2012.

Lemessy, K. G., Manohar, K., and Adeyanju, A.: Analysis of the Caribbean wave climate for wave energy harvesting, IET Renewable Power Generation, 15, 3409–3423, https://doi.org/10.1049/rpg2.12285, 2021.

Linscheid, N., Estupinan-Suarez, L. M., Brenning, A., Carvalhais, N., Cremer, F., Gans, F., Rammig, A., Reichstein, M., Sierra, C. A., and Mahecha, M. D.: Towards a global understanding of vegetation–climate dynamics at multiple timescales, Biogeosciences, 17, 945–962, https://doi.org/10.5194/bg-17-945-2020, 2020.

Ludka, B. C., Guza, R. T., O'Reilly, W. C., Merrifield, M. A., Flick, R. E., Bak, A. S., Hesser, T., Bucciarelli, R., Olfe, C., Woodward, B., Boyd, W., Smith, K., Okihiro, M., Grenzeback, R., Parry, L., and Boyd, G.: Sixteen years of bathymetry and waves at San Diego beaches, Scientific Data, 6, 161, https://doi.org/10.1038/s41597-019-0167-6, 2019.

Luijendijk, A., Hagenaars, G., Ranasinghe, R., Baart, F., Donchyts, G., and Aarninkhof, S.: The State of the World's Beaches, Scientific Reports, 8, 6641, https://doi.org/10.1038/s41598-018-24630-6, 2018.

Magar, V., Lefranc, M., Hoyle, R. B., and Reeve, D. E.: Spectral quantification of nonlinear behaviour of the nearshore seabed and correlations with potential forcings at Duck, NC, USA, Plos one, 7, e39 196, 2012.

Maraun, D. and Kurths, J.: Cross wavelet analysis: significance testing and pitfalls, Nonlinear Processes in Geophysics, 11, 505–514, https://doi.org/10.5194/npg-11-505-2004, 2004.

Marshall, G. J.: Trends in the Southern Annular Mode from Observations and Reanalyses, Journal of Climate, 16, 4134 – 4143, https://doi.org/10.1175/1520-0442(2003)016<4134:TITSAM>2.0.CO;2, 2003.

Martins, K., Blenkinsopp, C. E., Almar, R., and Zang, J.: The influence of swash-based reflection on surf zone hydrodynamics: a wave-by-wave approach, Coastal Engineering, 122, 27–43, https://doi.org/10.1016/j.coastaleng.2017.01.006, 2017.

McGlathery, K. J., Reidenbach, M. A., D'Odorico, P., Fagherazzi, S., Pace, M. L., and Porter, J. H.: Nonlinear Dynamics and Alternative Stable States in Shallow Coastal Systems, Oceanography, 26, 220–231, https://doi.org/10.5670/oceanog.2013.66, 2013.

Morales-Márquez, V., Cáceres-Euse, A., Hernández-Carrasco, I., Molcard, A., and Orfila, A.: Extreme waves in the Caribbean Sea: spatial regionalization and long-term analysis, Frontiers in Marine Science, 10, 1294 189, https://doi.org/10.3389/fmars.2023.1294189, 2023.

Nayfeh, A. H. and Mook, D. T.: Nonlinear oscillations, John Wiley & Sons, 2024.

Pikovsky, A., Rosenblum, M., and Kurths, J.: Synchronization, Cambridge university press, 12, 2001.

Pujol, M.-I., Faugère, Y., Taburet, G., Dupuy, S., Pelloquin, C., Ablain, M., and Picot, N.: DUACS DT2014: the new multi-mission altimeter data set reprocessed over 20 years, Ocean Science, 12, 1067–1090, https://doi.org/10.5194/os-12-1067-2016, 2016.

Purwanto, P., Sugianto, D. N., Zainuri, M., Permatasari, G., Atmodjo, W., Rochaddi, B., Ismanto, A., Wetchayont, P., and Wirasatriya, A.: Seasonal Variability of Waves Within the Indonesian Seas and Its Relation With the Monsoon Wind, ILMU KELAUTAN: Indonesian Journal of Marine Sciences, 26, 189–196, https://doi.org/10.14710/ik.ijms.26.3.189-196, 2021.

Roberts, J. and Roberts, T. D.: Use of the Butterworth low-pass filter for oceanographic data, Journal of Geophysical Research: Oceans, 83, 5510–5514, 1978.

Ruessink, B., Wijnberg, K., Holman, R., Kuriyama, Y., and Van Enckevort, I.: Intersite comparison of interannual nearshore bar behavior, Journal of Geophysical Research: Oceans, 108, 2003.

Sánchez-García, E., Palomar-Vázquez, J. M., Pardo-Pascual, J. E., Almonacid-Caballer, J., Cabezas-Rabadán, C., and Gómez-Pujol, L.: An efficient protocol for accurate and massive shoreline definition from mid-resolution satellite imagery, Coastal Engineering, 160, 103 732, 2020.

Sartini, L., Cassola, F., and Besio, G.: Extreme waves seasonality analysis: An application in the M editerranean S ea, Journal of Geophysical Research: Oceans, 120, 6266–6288, https://doi.org/10.1002/2015JC011061, 2015.

Semedo, A.: Seasonal Variability of Wind Sea and Swell Waves Climate along the Canary Current: The Local Wind Effect, Journal of Marine Science and Engineering, 6, https://doi.org/10.3390/jmse6010028, 2018.

Semedo, A., Soares, P. M., and Lemos, G.: Waves along Eastern boundary currents – The regional winds effect, Ocean Modelling, 129, 39–57, https://doi.org/https://doi.org/10.1016/j.ocemod.2018.07.005, 2018.

Shannon, C. E.: Communication in the presence of noise, Proceedings of the IRE, 37, 10–21, 2006.

Smith, R. K. and Benson, A. P.: Beach Profile Monitoring: How Frequent is Sufficient?, Journal of Coastal Research, pp. 573–579, http://www.jstor.org/stable/25736322, 2001.

Sterl, A. and Caires, S.: Climatology, variability and extrema of ocean waves: the Web-based KNMI/ERA-40 wave atlas, International Journal of Climatology, 25, 963–977, https://doi.org/10.1002/joc.1175, 2005.

Stuecker, M. F., Timmermann, A., Jin, F.-F., McGregor, S., and Ren, H.-L.: A combination mode of the annual cycle and the El Niño/Southern Oscillation, Nature Geoscience, 6, 540–544, 2013.

Takahashi, K., Montecinos, A., Goubanova, K., and Dewitte, B.: ENSO regimes: Reinterpreting the canonical and Modoki El Niño, Geophysical Research Letters, 38, https://doi.org/https://doi.org/10.1029/2011GL047364, 2011.

Tartini, G.: Trattato di musica seconda la vera scienza dell'armonia, Stamperia del Seminario, 1754.

Tomita, K.: 10. Periodically forced nonlinear oscillators, pp. 211–236, Princeton University Press, Princeton, ISBN 9781400858156, https://doi.org/doi:10.1515/9781400858156.211, 2014.

Torrence, C. and Compo, G. P.: A Practical Guide to Wavelet Analysis, Bulletin of the American Meteorological Society, 79, 61–78, https://doi.org/10.1175/1520-0477(1998)079<0061:APGTWA>2.0.CO;2, 1998.

Torrence, C. and Webster, P. J.: Interdecadal Changes in the ENSO–Monsoon System, Journal of Climate, 12, 2679 – 2690, https://doi.org/10.1175/1520-0442(1999)012<2679:ICITEM>2.0.CO;2, 1999.

Turki, I., Medina Santamaría, R., González Rodríguez, E. M., et al.: Beach memory, 2012.

Turner, I. L., Harley, M. D., Short, A. D., Simmons, J. A., Bracs, M. A., Phillips, M. S., and Splinter, K. D.: A multi-decade dataset of monthly beach profile surveys and inshore wave forcing at Narrabeen, Australia, Scientific Data, 3, 160 024, https://doi.org/10.1038/sdata.2016.24, 2016.

Turner, I. L., Harley, M. D., Almar, R., and Bergsma, E. W.: Satellite optical imagery in Coastal Engineering, Coastal Engineering, 167, 103 919, 2021.

Vitousek, S., Buscombe, D., Vos, K., Barnard, P. L., Ritchie, A. C., and Warrick, J. A.: The future of coastal monitoring through satellite remote sensing, Cambridge Prisms: Coastal Futures, 1, e10, 2023.

Vos, K., Harley, M. D., Splinter, K. D., Walker, A., and Turner, I. L.: Beach Slopes From Satellite-Derived Shorelines, Geophysical Research Letters, 47, e2020GL088 365, https://doi.org/10.1029/2020GL088365, 2020.

https://doi.org/10.5194/egusphere-2026-541
Preprint. Discussion started: 13 February 2026
© Author(s) 2026. CC BY 4.0 License.

Vos, K., Harley, M. D., Turner, I. L., and Splinter, K. D.: Pacific shoreline erosion and accretion patterns controlled by El Niño/Southern Oscillation, Nature Geoscience, 16, 140–146, 2023a.

Vos, K., Splinter, K. D., Palomar-Vázquez, J., Pardo-Pascual, J. E., Almonacid-Caballer, J., Cabezas-Rabadán, C., Kras, E. C., Luijendijk, A. P., Calkoen, F., Almeida, L. P., Pais, D., Klein, A. H. F., Mao, Y., Harris, D., Castelle, B., Buscombe, D., and Vitousek, S.: Benchmarking satellite-derived shoreline mapping algorithms, Communications Earth & Environment, 4, 345, https://doi.org/10.1038/s43247-023-01001-2, 2023b.

Warrick, J. A., Buscombe, D., Vos, K., Bryan, K. R., Castelle, B., Cooper, J. A. G., Harley, M. D., Jackson, D. W. T., Ludka, B. C., Masselink, G., Palmsten, M. L., Ruiz De Alegria-Arzaburu, A., Sénéchal, N., Sherwood, C. R., Short, A. D., Sogut, E., Splinter, K. D., Stephenson, W. J., Syvitski, J., and Young, A. P.: Coastal shoreline change assessments at global scales, Nature Communications, 15, 2316, https://doi.org/10.1038/s41467-024-46608-x, 2024.

Warrick, J. A., Buscombe, D., Vos, K., Kenyon, H., Ritchie, A. C., Harley, M. D., Janda, C., L'Heureux, J., and Vitousek, S.: Shoreline Seasonality of California's Beaches, Journal of Geophysical Research: Earth Surface, 130, e2024JF007 836, https://doi.org/10.1029/2024JF007836, 2025.

Wilks, D. S.: Principal component (EOF) analysis, in: International geophysics, vol. 100, pp. 519–562, Elsevier, 2011.

Wolter, K. and Timlin, M. S.: Measuring the strength of ENSO events: How does 1997/98 rank?, Weather, 53, 315–324, https://doi.org/https://doi.org/10.1002/j.1477-8696.1998.tb06408.x, 1998.